Title:

Lactate Accelerates Mouse ES Cell Differentiation Towards the XEN Lineage

Running Title:

Lactate Potentiates XEN induction *in vitro*

Authors/Affiliations:

Mohamed I. Gatie[1,2], Tyler T. Cooper[3,4,5], Gilles A. Lajoie[5,6], Gregory M. Kelly[1,2,3,6,7*]

Author List Footnotes:

[1] Department of Biology, Western University, London, ON, Canada

[2] Collaborative Specialization in Developmental Biology, Western University, London, ON, Canada

[3] Department of Physiology and Pharmacology, Western University, London, ON, Canada

[4] Molecular Medicine Research Laboratories, Krembil Centre for Stem Cell Biology, Robarts Research Institute, London, Ontario, Canada

[5] Department of Biochemistry, Don Rix Protein Identification Facility, Lawson Health Research Institute, Western University, London, Ontario, Canada

[6] Lawson Health Research Institute, Western University, London, ON, Canada

[7] Child Health Research Institute, London, ON, Canada

Contact information:

[*]Correspondence: gkelly@uwo.ca

Summary:

Metabolism plays a crucial role for cell survival and function; however, recent evidence has implicated it in regulating embryonic development. The inner cell mass undergoes orchestrated cellular divisions resulting in the formation of embryonic stem cells and extraembryonic endoderm (XEN) cells. Concomitantly, changes in the metabolic profile occurs during development and are well-documented in the embryonic lineages. However, a comprehensive multi-omics analysis of these features in XEN cells remains lacking. We observed that feeder-free XEN cells exhibited high sensitivity to glycolytic inhibition in addition to maintaining elevated intra- and extracellular lactate levels. XEN cells maintain high lactate levels by increased LDHA activity and re-routing pyruvate away from the mitochondria. Importantly, exogenous lactate supplementation or promoting intracellular lactate accumulation enhances XEN differentiation *in vitro*. Our results highlight how lactate contributes to XEN differentiation in the mammalian embryo and may serve to enhance reprogramming efficiency of cells used for regenerative medicine.

Highlights:

- Feeder-free XEN cells exhibit high sensitivity to glycolytic inhibition
- Distinct transcriptomic, proteomic and metabolomic profile exists between feeder-free ES and XEN cells
- Elevated intracellular and extracellular lactate is observed in feeder-free XEN cells
- Lactate enhances feeder-free XEN differentiation *in vitro*

Keywords:

Embryonic stem cells

Extraembryonic endoderm cells

Pluripotency

Differentiation

Glycolysis

Oxidative Phosphorylation

Metabolites

Lactate

49 # Introduction

50 The early mammalian blastocyst is comprised of two distinct layers: the inner cell
51 mass (ICM) and trophectoderm. The ICM houses embryonic stem (ES) cells and primitive
52 endoderm cells, and the latter differentiate into parietal and visceral endoderm cells.
53 Collectively primitive, parietal and visceral endoderm cells make up the extraembryonic
54 endoderm (XEN) lineage. Various ES cells have been cultured at different developmental
55 time-points (Evans and Kaufman, 1981), each requiring specific conditions. For instance,
56 preimplantation ICM cells represent a “naïve” state and can be artificially maintained
57 under LIF and serum/BMP (Nichols et al., 1990) or defined conditions of LIF-2i in N2B27
58 media where dual inhibition of glycogen synthase kinase 3 and mitogen-activated protein
59 kinase pathways maintain pluripotency (Ying et al., 2008). However, the post-implantation
60 or “primed” epiblast stem cells, which are poised to give rise to the embryo proper, require
61 Activin A and FGF2 in culture (Brons et al., 2007). In addition to differences in culture
62 conditions, both naïve and primed states differ in their expression profile of pluripotency
63 core genes, DNA methylation, histone modification status, clonogenicity and chimera
64 contribution (Davidson et al., 2015). XEN cells, which contribute to both embryonic and
65 extraembryonic endoderm tissue (Nowotschin et al., 2019), have been derived by
66 isolation from blastocyst (Niakan et al., 2013), differentiated using exogenous factors
67 (Anderson et al., 2017; Cho et al., 2012; Soprano et al., 2007), reprogrammed from
68 fibroblast cells (He et al., 2020; Parenti et al., 2016), or form after the overexpression of
69 *Gata4/6* (Fujikura et al., 2002; Shimosato et al., 2007) or *Sox17* (McDonald et al., 2014).
70 In addition, evidence indicates that the metabolic state between embryonic and

71 extraembryonic lineages differs, suggesting that metabolism may be sufficient to
72 influence lineage commitment.

73 Naïve ES cells exhibit a bivalent metabolic profile, relying on glycolysis and
74 oxidative phosphorylation (OXPHOS) to generate energy, while epiblast stem cells are
75 exclusively glycolytic, despite displaying a mature mitochondrial ultrastructure (Zhou et
76 al., 2012). Although the majority of studies have focused on naïve and primed ES cells,
77 recent reports on extraembryonic cells show they are reliant on OXPHOS metabolism
78 (Choi et al., 2020), with a similar mitochondrial ultrastructure to epiblast stem cells (Seo
79 et al., 2020; Zhou et al., 2012). However, details on the comprehensive intracellular profile
80 of metabolites and their role during differentiation remains unknown.

81 Small metabolites have garnered attention with their role in maintaining
82 pluripotency, promoting differentiation and enhancing reprogramming efficiency of
83 induced pluripotent stem cells (Mathieu and Ruohola-Baker, 2017; Tsogtbaatar et al.,
84 2020; Zhang et al., 2012). These small compounds play integral roles in energy
85 production and epigenetic modifications. For instance, short-chain and saturated fatty
86 acids can modulate histone deacetylases and the epigenetic landscape and thus are
87 implicated in enhancing the efficiency of stem cell differentiation (Mali et al., 2010; Yanes
88 et al., 2010). Also, the depletion of threonine or loss of threonine dehydrogenase (TDH)
89 impacts stemness (Wang et al., 2009), while supplementation of L-threonine maintains
90 pluripotency (Ryu and Han, 2011). Therefore, naturally occurring metabolites play an
91 important role in regulating pluripotency and differentiation of stem cells by modulating
92 the metabolic and epigenetic landscape.

93 In this report we used a multi-omics approach to identify metabolic changes in cells
94 of the ICM and have further characterized the metabolic pathways involved in regulating
95 XEN lineage commitment. Overall, we observed a significant reduction in the survival of
96 feeder-free XEN cells following glycolytic inhibition. Transcriptomic and proteomic
97 profiling implicate lactate metabolism in regulating the differentiation towards the XEN
98 lineage. Strikingly, lactate was enriched intra- and extracellularly in feeder-free XEN cells,
99 and promoting intracellular lactate accumulation or supplementing with exogenous L-
100 lactate enhanced XEN induction. Together our results elucidate an unacknowledged role
101 for lactate in cell differentiation and fate commitment in the early mammalian embryo.

102 # Results

103 **ES cells are less sensitive to glycolytic inhibition than XEN cells**

104 A recent report characterized the metabolic profile of XEN cells as reliant on
105 OXPHOS metabolism (Choi et al., 2020). Albeit informative, this study derived and
106 maintained XEN cells on inactivated mouse embryonic fibroblasts, which are oxidative in
107 nature (Folmes et al., 2011) and are known to reduce the reliance of pluripotent stem
108 cells on glycolysis (Gu et al., 2016). To address if culturing methods influence the
109 metabolic profiles, ES-E14TG2a embryonic stem cells (ES cells) and extraembryonic
110 endoderm cells (XEN cells) (Kunath et al., 2005) were cultured under feeder-free
111 conditions in media containing 50mM 2-Deoxy-D-glucose (2-DG; glycolysis inhibitor) or
112 2.5μM oligomycin (OXPHOS inhibitor), and results were compared with cells grown under
113 control conditions (Figure 1). ES cells displayed domed-homogenous colonies while XEN
114 cells were single-celled, with two distinct morphologies present in culture, spindle-like or
115 round and refractile in nature (Figure 1A, Figure S1A).

116 ES colony shape appeared to be insensitive to 2-DG and oligomycin treatment;
117 however, XEN cells lost their distinct morphologies, particularly in the 2-DG treatment and
118 adopted a spindle-like morphology, indicative of cell stress (Figure 1A). In contrast to a
119 previous report (Choi et al., 2020), XEN cells were more sensitive to glycolytic inhibition
120 (5.87% ± 1.82) than OXPHOS inhibition with oligomycin (41.3% ± 7.30; $P < 0.01$; Figure
121 1B). Since ES cells are metabolically bivalent (Zhou et al., 2012), the significant reduction
122 in cell viability under both treatments was expected ($P < 0.01$) and not significant between
123 the two treatments (2-DG: 45.3% ± 8.84 *versus* oligomycin: 62.7% ± 5.24; Figure 1B).
124 Despite this reduction in cell viability, no change in relative total ATP levels was observed

125 between the two populations and treatments (Figure 1C). Collectively, our findings
126 support the notion that feeder-free XEN cells are more sensitive to glycolytic inhibition
127 than feeder-free ES cells.

128 **Intracellular metabolomic profiling of ICM cells**

129 Since feeder-free ES and XEN cells responded differently to metabolic inhibitors,
130 we exploited the feeder-free system to identify changes in intracellular metabolites
131 between the two populations. For metabolite identification, untargeted metabolomics was
132 used to measure the relative levels of intracellular metabolites (Figure 2). We identified
133 142 intracellular metabolites of which 18 were significantly enriched in ES cells and 68 in
134 XEN cells (Table 1; Figure 2A). Next, targeted metabolomics was performed to quantify
135 the levels of amino acids (Figure 2B) and metabolites involved in glycolysis and the
136 tricarboxylic acid (TCA) cycle (Figure 2C). Several amino acids were significantly
137 enriched in XEN cells, including proline, serine and threonine, which are reported to play
138 a role in pluripotency and differentiation (Baksh et al., 2020; Comes et al., 2013; Ryu and
139 Han, 2011; Wang et al., 2009). While most metabolites involved in glycolysis and TCA
140 cycle were not statistically significant, intracellular lactate and 2-hydroxyglutarate were
141 significantly higher in XEN cells when compared with ES cells ($P < 0.05$; Figure 2C).
142 Together, our data indicate that XEN cells exhibit a unique metabolite profile that is
143 distinct from the ES population.

144 **Transcriptomic and proteomic analysis showcases the importance of metabolic**
145 **pathways during embryonic development**

146 Bulk transcriptomic and proteomic analyses were performed on ES and XEN cells
147 in order to compare global gene expression and protein abundance patterns and assign

148 molecular pathway(s) to the metabolite profiles. Results revealed 2742 genes (Figure 3A)
149 and 165 proteins (Figure 3B) significantly upregulated in the ES population. In contrast,
150 1716 genes (Figure 3A) and 298 proteins (Figure 3B) were significantly upregulated in
151 XEN cells. As expected, markers of pluripotency including *Nanog*, *Sox2*, OCT4 and
152 ESRRB were enriched in the ES population, while XEN markers such as *Gata4/6*,
153 *Sox7/17*, *Dab2*, and PDGFRA were significantly enriched in XEN cells (Figure 3A, B).
154 Differentially expressed genes and proteins enriched in either ES or XEN cells were
155 selected and analyzed by gene ontology to classify targets based on their biological
156 process (Figure S2A-D), cellular compartment (Figure S2E-H) and molecular process
157 (Figure S2I-L). As expected, targets from ES cells were enriched for biological processes
158 associated with multicellular organism development and regulation of transcription
159 (Figure S3A, B). Conversely, XEN cells terms were associated with various signaling
160 pathways, endodermal development and extracellular matrix organization (Figure S3C,
161 D).

162 Kyoto Encyclopedia of Genes and Genomes (KEGG) enrichment analysis was
163 also performed on genes and proteins to identify biological pathways specific to each
164 population (Figure 3C-G). XEN cells expressed targets primarily involved in proteoglycan
165 metabolism and endoplasmic reticulum processing (Figure 3F, G, S3G, H), as reported
166 previously (Choi et al., 2020). However, metabolism of xenobiotics by cytochrome P450
167 and glucose/pyruvate metabolism were enriched in the ES population and represent two
168 common KEGG pathways between the RNAseq and MS datasets (Figure 3C, D).
169 Interestingly, three targets that were highly enriched in both datasets and linked to
170 glucose metabolism were aldehyde dehydrogenase 1 family member B1 (ALDH1B1),

171 phosphoenolpyruvate carboxykinase 2 (PCK2) and lactate dehydrogenase B (LDHB,
172 Figure 3E). Together, this data would suggest that these targets and their metabolites
173 play a role in either maintaining pluripotency or in the differentiation towards the XEN
174 lineage.

175 **Enzymes involved in lactate homeostasis are upregulated in feeder-free XEN cells**

176 Pyruvate is converted into lactate by the activity of LDHA and converted back by
177 LDHB; since the latter was enriched in the ES population (Figure 3A-E), and lactate was
178 enriched in XEN cells intracellularly (Figure 2C), we sought to further investigate the
179 levels of enzymes involved in lactate metabolism. qRT-PCR results showed significantly
180 higher *Ldha*/*Ldhb* expression in XEN cells compared with ES cells ($P < 0.01$, Figure 4A),
181 and this was confirmed at the protein level using immunoblot analysis (Figure 4B).
182 Extracellular lactate levels were also measured, and results showed significantly higher
183 levels in XEN cells ($P < 0.05$, Figure 4C). Furthermore, the expression of the lactate
184 transporter *Mct1* (Figure 4D), but not *Mct4* (Figure 4E), was significantly upregulated in
185 XEN cells ($P < 0.0001$) and is a prime candidate linked to these high extracellular lactate
186 levels. Pyruvate can also be oxidized in the mitochondria by the pyruvate dehydrogenase
187 complex (PDC) to generate acetyl-CoA. This conversion is dependent on the activity of
188 the PDC, which is negatively regulated by phosphorylation of the E1α subunit by
189 members of the pyruvate dehydrogenase kinase (PDK) family. Expression analysis
190 shows that *Pdk1, 2* and *4,* but not *Pdk3,* were significantly downregulated in XEN cells
191 (Figure 4F-I). Similarly, immunoblot analysis revealed low levels of PDC-E1α$^{Ser232/Ser293}$ in
192 XEN cells (Figure 4J), indicating that the PDC is active and would suggest higher
193 OXPHOS activity. However, expression analysis of the mitochondrial pyruvate carriers

194 *Mpc1* (Figure 4K), but not *Mpc2* (Figure 4L), showed significantly reduced expression in
195 XEN cells ($P < 0.0001$). Thus, despite having an active PDC, pyruvate in XEN cells fails
196 to enter the mitochondria, and instead is preferentially converted to lactate by the
197 enhanced LDHA activity (Figure 4A, B). These results would suggest that lactate
198 participates in specifying ES cells towards a XEN lineage.

199 **Promoting intracellular lactate enhances XEN differentiation**

200 Given the previous data highlighting a potential role for lactate in XEN cells (Figure
201 1-4), we sought to directly assess whether modulating lactate metabolism had an effect
202 on XEN induction *in vitro* (Figure 5). We adopted a previously defined chemical cocktail
203 (Anderson et al., 2017) to induce naïve mouse ES cells towards the XEN lineage.
204 Exogenous supplementation of LIF, Activin A and CHIR99021 (inhibitor of glycogen
205 synthase kinase 3) in the absence of insulin (Figure S3A) promotes differentiation towards
206 the XEN lineage as evident by elevated *Gata6* and *Dab2* transcript and low levels of
207 *Nanog* and *Oct4* (Figure S3B-E). To test whether lactate metabolism plays a role in XEN
208 differentiation, we used two approaches. In the first, three inhibitors were selected, two of
209 which would promote intracellular lactate accumulation (UK5099 and AZD3965), while
210 the other would promote pyruvate uptake into the mitochondria (Dichloroacetate, DCA).
211 In the second approach, media was supplemented with exogenous L-lactate and cells
212 were assessed for markers of pluripotency and XEN differentiation. UK5099 is a potent
213 pan MPC inhibitor that prevents pyruvate uptake into the mitochondria (Halestrap, 1975;
214 Vacanti et al., 2014), while AZD3965, a highly-specific MCT1 inhibitor, reduces lactate
215 secretion in human stem cells (Gu et al., 2016) and cancer cells (Polanski et al., 2014).
216 The latter was used since MCT1 is the predominant transporter responsible for exporting

217 lactate extracellularly in XEN cells (Figure 4D). Generally, neither UK5099, AZD3965 or
218 L-lactate affected *Oct* or *Nanog* expression (Figure 5C, F, G, J, K); however, *Oct4*
219 expression was slightly but significantly downregulated ($P < 0.05$) in ES cells cultured
220 under 2i-LIF and UK5099 conditions (Figure 5B). In contrast, DCA-treated ES cells
221 cultured with 2i-LIF had slightly elevated *Oct4* and *Nanog* expression when compared to
222 controls (Figure 5N, O).

223 Next, ES cells were induced towards the XEN lineage under control conditions or
224 treated with inhibitors or supplemented with L-lactate. ES cells treated with UK5099 in
225 XEN induction media were not viable after 48h post treatment (Figure 5D, E), while
226 surprisingly those cultured with either AZD3965 (Figure 5H, I) or supplemented with L-
227 lactate (Figure 5L, M) for 96h showed enhanced *Gata6* and *Dab2* expression when
228 compared to controls. Prolonged L-lactate supplementation induced cell death at 10 days
229 post treatment in cells differentiated towards the XEN lineage (data not shown).
230 Conversely, when ES cells were treated with DCA in XEN induction media, thereby
231 promoting pyruvate uptake into the mitochondria and reducing intracellular lactate, *Gata6*
232 and *Dab2* expression were significantly downregulated when compared to controls ($P <$
233 0.05, Figure 5P, Q). Therefore, promoting intracellular lactate accumulation enhanced
234 XEN induction *in vitro*, highlighting a novel role for lactate as a signaling molecule involved
235 in the differentiation of XEN cells.

236 # Discussion

237 We have shown previously that F9 embryonal carcinoma cells mimic the transition
238 to a XEN-like lineage when co-treated with retinoic acid and a cAMP analog, and more
239 importantly, these cells exhibited a metabolic phenotype reliant exclusively on glycolysis
240 (Gatie and Kelly, 2018). While recent reports have expanded on the metabolic profiles
241 observed in the early embryonic lineages (Choi et al., 2020; Zhou et al., 2012), a
242 comprehensive analysis of the metabolites and their roles during development remains
243 lacking. Our data indicates that feeder-free XEN cells are sensitive to glycolytic inhibition
244 when compared with OXPHOS inhibition (Figure 1A, B). This phenomenon is also
245 observed in mouse primed stem cells, human stem cells (Zhou et al., 2012) and canine
246 epiblast stem cells (Tobias et al., 2018), suggesting that these characteristics are
247 adaptive mechanisms linked to a developmental stage. Furthermore, XEN cells possess
248 altered glycolytic enzyme levels involved in pyruvate and lactate homeostasis (Figure 4).
249 Recent reports suggested that XEN cells rely on OXPHOS metabolism for energetic
250 needs (Choi et al., 2020); however, the developmental stage and culture condition of XEN
251 cells may influence their metabolic profile. For instance, primitive endoderm cells are
252 present within the ICM at 3.5 days post fertilization and they further commit into parietal
253 and visceral endoderm cells shortly after implantation. A similar phenomenon is observed
254 between preimplantation naïve *versus* post-implantation primed ES cells, which display
255 distinct metabolic profiles (Zhou et al., 2012), suggesting that XEN cells may exhibit a
256 unique metabolic signature depending on their developmental stage. In addition, the
257 localization of XEN cells varies depending on the stage of development, where primitive
258 endoderm cells reside within the ICM, visceral endoderm cells surround the epiblast while

259 parietal endoderm cells interact with trophoblast stem cells and undergo an epithelial-to-
260 mesenchymal transition and migrate along the inner surface of the trophectoderm (Hogan
261 et al., 1980). Therefore, the precise identity of these XEN cells and their interaction with
262 the microenvironment may influence their metabolic needs. Lastly, culture conditions vary
263 between trophoblast, ES and XEN cells, and its known that the latter can be derived using
264 various culture conditions and supplements (Anderson et al., 2017; Cho et al., 2012;
265 Fujikura et al., 2002; He et al., 2020; Kunath et al., 2005; McDonald et al., 2014; Niakan
266 et al., 2013; Paca et al., 2012; Shimosato et al., 2007; Soprano et al., 2007; Wamaitha et
267 al., 2015). Together, the ability to derive XEN cells by various means would contribute to
268 their heterogeneity (Kunath et al., 2005; Paca et al., 2012) and potentially affect the
269 metabolic profile of these cells. For example, XEN cells can be generated by the
270 overexpression of *Gata4* in ES cells (Fujikura et al., 2002; Wamaitha et al., 2015) or
271 reprogramming fibroblasts using a chemical cocktail (He et al., 2020). While both methods
272 result in the establishment of XEN cells, *Gata4*-induced ES cells display gradual reduction
273 in hexokinase 2 (HK2) and glucose transporter 1 (GLUT1) levels (Mulvey et al., 2015),
274 while XEN cells reprogrammed from fibroblasts display elevated *Hk2* and *Glut1* levels
275 (He et al., 2020). Together, these differences highlight the metabolic complexity and
276 plasticity of all cells in the developing embryo, and in XEN cells specifically.

277 As the embryo develops its metabolic needs shift to meet energetic demands for
278 growth and development and this metabolic rewiring is dependent on extrinsic and
279 intrinsic cues. The blastocyst resides in a hypoxic environment, with oxygen tension
280 dropping significantly during implantation (Fischer and Bavister, 1993). This hypoxic
281 environment results in the stabilization of hypoxia-inducible factor one alpha (HIF1α),

282 resulting in the increase in enzymes shifting the metabolic profile towards glycolysis.
283 During implantation, however, angiogenesis promotes reoxygenation of the embryo
284 triggering a switch to OXPHOS. Despite residing in a similar environment, trophoblast
285 stem cells rely on OXPHOS metabolism, largely to fuel the sodium/potassium ion pumps
286 required for blastocoel expansion (Houghton et al., 2003). While extrinsic factors such as
287 the microenvironment are important, intrinsic factors play a key role in remodeling
288 metabolic needs to meet developmental programs. For example, naïve ES cells are
289 metabolically flexible and utilize both glycolysis and OXPHOS metabolism. However, the
290 transition to a primed state is marked by a switch to glycolytic metabolism, which is largely
291 due to HIF1α stabilization within the cell (Zhou et al., 2012). While changes in the levels
292 of metabolic enzymes play a role in remodelling cellular metabolism, the metabolites
293 resulting from the activity of these enzymes are instrumental in regulating pluripotency
294 and/or differentiation. Our study is the first to provide a comprehensive snapshot of the
295 intracellular metabolite profile of feeder-free XEN cells and reveals how elevated levels
296 of key metabolites, mainly lactate, influence differentiation.

297 Lactate, the primary source of carbon for the TCA cycle in both normal and cancer
298 tissues (Hui et al., 2017), is generated by the activity of LDHA, reportedly enriched in XEN
299 cells (Figure 4A, B). Since lactate can be converted to pyruvate by LDHB, the
300 stoichiometric ratio between the two isoforms dictates the fate of pyruvate and lactate. In
301 addition, the oxidation of pyruvate by the PDC is required for its conversion to acetyl CoA,
302 and the activity of the complex is regulated by the PDK family. Despite detecting elevated
303 intracellular (Figure 2C) and extracellular (Figure 4C) lactate levels in XEN cells, the PDC
304 was not phosphorylated and is therefore active in XEN cells (Figure 4J). While reduced

305 expression of *Mpc1* was found in XEN cells (Figure 4K), which may explain the rerouting
306 of pyruvate to lactate, PDC is known to have moonlighting abilities and can translocate to
307 the nucleus where it generates acetyl CoA for acetylation of H3K9 and H3K18 (Sutendra
308 et al., 2014). Thus, since total lysates were used to analyze the phosphorylation status of
309 the PDC in ES and XEN cells, it is possible that a higher proportion of the active complex
310 is nuclear and not mitochondrial. Nevertheless, since elevated intracellular lactate levels
311 were found in XEN cells (Figure 2C), it was hypothesized that lactate plays a crucial role
312 during XEN differentiation. Chemical inhibition to promote intracellular lactate
313 accumulation (Figure 5H, I) or supplementation of XEN induction media with L-lactate
314 (Figure 5L, M) showed enhanced XEN differentiation. Surprisingly, blocking pyruvate
315 uptake into the mitochondria using UK5099 led to cell mortality (Figure 5D, E).
316 Alternatively, promoting pyruvate uptake into the mitochondria by inhibiting PDKs resulted
317 in significant reduction in XEN differentiation (Figure 5P, Q). Therefore, our results
318 support the notion that maintaining intracellular lactate levels potentiates ES cells towards
319 a XEN lineage. Since lactate can stabilize HIF1α and promote a glycolytic phenotype (De
320 Saedeleer et al., 2012), the lactate-HIF1α axis may provide a mechanism for XEN
321 differentiation. In addition, lactate can also inhibit histone deacetylases (Latham et al.,
322 2012), and in conjunction with active PDC (Figure 4J), promote hyperacetylation, which
323 we observed in XEN cells (data not shown). Thus, it appears lactate is a key player linking
324 metabolism with epigenetic factors and transcription. These links provide insight into the
325 role lactate plays in directing the differentiation of XEN cells, and together they
326 underscore the importance of how the metabolic profile directs lineage commitment within
327 the mouse early embryo.

328 # Experimental Procedures

329 **ES, XEN and cXEN Cell Culture**

330 The ES-E14TG2a embryonic stem (ES) cells were obtained from the University of
331 California, Davis. ES cells were cultured feeder-free on 0.1% gelatin-coated tissue culture
332 plates in ES media: 50/50 neurobasal/DMEM-F12 media (Thermo Fisher), 1X N2
333 supplement (Thermo Fisher), 0.5X B27 (without retinoic acid; Thermo Fisher), 2mM
334 GlutaMAX™ (Thermo Fisher), 0.1mM β-mercaptoethanol (Thermo Fisher), 100U/ml units
335 of LIF (Millipore-Sigma), 3μM CHIR99021 (ApexBio) and 1μM PD 0325901 (ApexBio).
336 ES cells were passaged every 3–4 days using Accutase (Thermo Fisher) and used to
337 passage 30. ES media was changed daily to maintain optimal growth and reduce
338 spontaneous differentiation. E4 extraembryonic endoderm (XEN) cells, generously
339 donated from Dr. Janet Rossant, University of Toronto (Kunath et al., 2005), were cultured
340 in RPMI1640 media (Thermo Fisher) supplemented with 15% fetal bovine serum (Thermo
341 Fisher), 2mM GlutaMAX™ and 0.1mM β-mercaptoethanol. XEN cells were passaged
342 every 2–4 days using TrypLE Express (Thermo Fisher) up to passage 20.

343 Chemically induced XEN (cXEN) differentiation was performed following a previously
344 established protocol (Anderson et al., 2017). Briefly, ES cells were seeded onto 0.1%
345 gelatin-coated tissue culture plates in base XEN media (RPMI1640 media, 0.5X B27
346 without insulin, 2mM GlutaMAX™ and 0.1mM β-mercaptoethanol) for 2 days. To induce
347 XEN differentiation, base XEN media was supplemented with 100U/ml units of LIF, 3μM
348 CHIR99021 and 20ng/ml Activin A (R&D Systems), which was changed every 2 days. All
349 lines were grown at 37°C and 5% CO_2 and checked for chromosomal abnormalities and
350 mycoplasma (Dobrovolny and Bess, 2011) at the beginning of the project.

351 **RNA Isolation, cDNA synthesis and qRT-PCR analysis**

352 RNA was extracted from cells using QIAshredder/RNAeasy Mini kit (Qiagen) and reverse
353 transcribed into cDNA using the High-Capacity cDNA Reverse Transcription kit (Thermo
354 Fisher). For quantitative RT-PCR, reactions contained 500nM of forward and reverse
355 primers (Gatie and Kelly, 2018), SensiFAST SYBR Mix (FroggaBio), and cDNA.
356 Reactions were run on a CFX Connect Real-Time PCR detection system (Bio-Rad), and
357 results presented using the comparative cycle threshold ($2^{-\Delta\Delta Ct}$) method with *Rpl14*
358 serving as the internal control.

359 **RNA Sequencing Analysis**

360 Total RNA was extracted as described previously and quantified using a NanoDrop 2000
361 spectrophotometer (Thermo Fisher) and Agilent 2100 bioanalyzer (Agilent Technologies).
362 Library construction and sequencing were performed using the BGISEQ-500 platform
363 (Beijing Genome Institute). Clean reads were mapped to a reference genome using
364 Bowtie2 (Langmead and Salzberg, 2012) and gene expression levels were calculated
365 with RSEM (Li and Dewey, 2011). Differentially expressed genes were detected with
366 DEseq2 (Love et al., 2014) with fold change ≥ 2.0 and $P \leq 0.0001$, and GO-term
367 enrichment and KEGG analyses were conducted using David v6.8 (Huang da et al.,
368 2009a, b).

369 **Protein extraction, quantification and immunoblot analysis**

370 Total cell lysates were harvested using RIPA buffer supplemented with protease and
371 phosphatase inhibitors (Thermo Fisher). Protein concentrations were quantified using a
372 DC™ protein assay (Bio-Rad). Approximately 5–20μg of protein was separated on 5–15%
373 polyacrylamide gels at 100V, then transferred onto PVDF membranes (Bio-Rad)

374 overnight at 4°C at 20V. Membranes were washed in TBS-T with 0.1% Tween-20 and
375 blocked with 5% skim milk powder for 30 minutes at room temperature with gentle shaking.
376 Membranes were probed with primary antibodies (Gatie and Kelly, 2018) overnight at 4°C
377 followed by washes with TBS-T and secondary antibody incubation for 2 hours at room
378 temperature. Images were captured using a ChemiDoc™ Touch Imaging System (Bio-
379 Rad).

380 **Proteomic Analysis**

381 Sample preparation, handling and quantification were performed according to (Cooper et
382 al., 2018). Briefly, cells were pelleted and 50µg of protein was quantified by ionic
383 detergent compatible Pierce 660nm Protein Assay Reagent (Thermo Fisher) in 8M Urea,
384 50mM ammonium bicarbonate, 10mM dithiothreitol, and 2% SDS lysis buffer. Lysates
385 were sonicated, reduced and alkylated followed by precipitation in chloroform/methanol
386 (Wessel and Flugge, 1984), and digested samples were resuspended in 0.1% formic acid
387 in preparation for LC-MS/MS. One microgram of tryptic peptides was injected into a
388 Waters nano-Acquity HPLC system (Waters, Milford, MA) coupled to an ESI Orbitrap
389 mass spectrometer (Orbitrap Elite or QExactive, ThermoFisher Scientific). MS raw files
390 were examined using MaxQuant (1.6.5.0) and the Human Uniprot database. Bioinformatic
391 analyses were performed in Perseus (1.5.8.5), and statistical analyses performed using
392 multiple sample t-test with a permutation FDR set at 0.05. GO-term enrichment and
393 KEGG analyses were conducted using David v6.8 (Huang da et al., 2009a, b).

394 **Detection of Total ATP levels**

395 Total ATP levels were measured using the CellTiter-Glo® Luminescent Cell Viability
396 Assay (Promega). Cells were detached and re-suspended in media and aliquoted into

397 96-well plate. Cells were lysed in CellTiter-Glo® reagent, incubated in the dark for 10
398 minutes, and luminance recorded using a Modulus™ II microplate multimode system
399 (Promega).

400 **Detection of Extracellular Lactate Levels**

401 Cells were cultured under normal conditions until reaching 70% confluency. Media from
402 each cell population was collected, centrifuge at 14000g at 4°C for 10 minutes and
403 analyzed using a BioProfile®400 Chemical Analyzer (Nova Biochemical), at the GCRC
404 Metabolomics Core Facility, McGill University. Values were normalized to protein
405 concentrations.

406 **Metabolomic Analysis**

407 Three million cells, cultured for 4 days under normal conditions, per sample were used
408 for extraction and analysis. Samples were analyzed for metabolites involved in glycolysis,
409 and TCA cycle, as well as amino acids, fatty acid and lipids. Sample preparation, handling
410 and quantification were carried out as in (Yuan et al., 2012) by The Analytical Facility for
411 Bioactive Molecules, The Hospital for Sick Children, Toronto, Canada. Briefly, cells were
412 harvested in 80% methanol (vol/vol) solution, centrifuged at 14,000g for 5 minutes at 4°C.
413 Samples were aliquoted and lyophilized prior to injection. Approximately 20µl of LC/MS
414 grade water was used to resuspend samples and 5–10µl was injected into a LC-MS/MS
415 system which was a SCIEX 5500 QTRAP mass spectrometer (SCIEX) coupled with an
416 Agilent 1290 HPLC stack (Agilent Technologies). MultiQuant (v3.0; SCIEX) was used for
417 analysis,

418 **Data and Code Availability**

419 Data files can be obtained from accession number GEO: GSE159855.

420 **Statistical Analysis**

421 All values are presented as mean ± SEM from at least three biological experiments. In
422 some instances (TEM experiments), three technical replicates were also included.
423 Comparisons between two groups were performed using Student's t-test, while
424 comparisons between three or more groups were done using an ANOVA test followed by
425 Tukey's honest significant difference test. All graphs and statistics were generated using
426 Prism (v8.4.3). *P*-values were considered significant at $^{*}P<0.05$, $^{**}P<0.01$, $^{***}P<0.001$,
427 $^{****}P<0.0001$.

Acknowledgments:

This work was supported by discovery grant from the Natural Sciences and Engineering Research Council (NSERC R2615A02) to G.M.K. G.A.L. was supported by NSERC and Canadian Foundation for Innovation (CFI). M.I.G was supported by NSERC CGS-D scholarship and the Child Health Research Institute. The authors acknowledge the assistance from the GCRC Metabolomics core facilities, which is supported by grants from CFI, Canadian Institutes of Health Research, and Terry Fox Research Institute. The authors wish to thank Ashley St. Pierre of The Analytical Facility for Bioactive Molecules, The Hospital for Sick Children, Toronto, Canada for assistance with metabolite identification and analysis.

Author Contributions:

MIG conceptualized, designed, performed the experiments and wrote the manuscript. TTC performed and analyzed proteomics experiment.

GAL managed the proteomic component of the project.

GMK was involved with MIG and the experimental design and supervised the research.

Declaration of Interests:

The authors declare no interest.

445 **References:**

446 Anderson, K.G.V., Hamilton, W.B., Roske, F.V., Azad, A., Knudsen, T.E., Canham,
447 M.A., Forrester, L.M., and Brickman, J.M. (2017). Insulin fine-tunes self-renewal
448 pathways governing naive pluripotency and extra-embryonic endoderm. Nat Cell Biol
449 *19*, 1164-1177.
450 Baksh, S.C., Todorova, P.K., Gur-Cohen, S., Hurwitz, B., Ge, Y., Novak, J.S.S.,
451 Tierney, M.T., Dela Cruz-Racelis, J., Fuchs, E., and Finley, L.W.S. (2020). Extracellular
452 serine controls epidermal stem cell fate and tumour initiation. Nat Cell Biol *22*, 779-790.
453 Brons, I.G., Smithers, L.E., Trotter, M.W., Rugg-Gunn, P., Sun, B., Chuva de Sousa
454 Lopes, S.M., Howlett, S.K., Clarkson, A., Ahrlund-Richter, L., Pedersen, R.A.*, et al.*
455 (2007). Derivation of pluripotent epiblast stem cells from mammalian embryos. Nature
456 *448*, 191-195.
457 Cho, L.T., Wamaitha, S.E., Tsai, I.J., Artus, J., Sherwood, R.I., Pedersen, R.A.,
458 Hadjantonakis, A.K., and Niakan, K.K. (2012). Conversion from mouse embryonic to
459 extra-embryonic endoderm stem cells reveals distinct differentiation capacities of
460 pluripotent stem cell states. Development *139*, 2866-2877.
461 Choi, J., Seo, B.J., La, H., Yoon, S.H., Hong, Y.J., Lee, J.H., Chung, H.M., Hong, K.,
462 and Do, J.T. (2020). Comparative analysis of the mitochondrial morphology, energy
463 metabolism, and gene expression signatures in three types of blastocyst-derived stem
464 cells. Redox Biol *30*, 101437.
465 Comes, S., Gagliardi, M., Laprano, N., Fico, A., Cimmino, A., Palamidessi, A., De
466 Cesare, D., De Falco, S., Angelini, C., Scita, G.*, et al.* (2013). L-Proline induces a

467 mesenchymal-like invasive program in embryonic stem cells by remodeling H3K9 and
468 H3K36 methylation. Stem Cell Reports *1*, 307-321.
469 Cooper, T.T., Sherman, S.E., Kuljanin, M., Bell, G.I., Lajoie, G.A., and Hess, D.A.
470 (2018). Inhibition of Aldehyde Dehydrogenase-Activity Expands Multipotent Myeloid
471 Progenitor Cells with Vascular Regenerative Function. Stem Cells *36*, 723-736.
472 Davidson, K.C., Mason, E.A., and Pera, M.F. (2015). The pluripotent state in mouse and
473 human. Development *142*, 3090-3099.
474 De Saedeleer, C.J., Copetti, T., Porporato, P.E., Verrax, J., Feron, O., and Sonveaux,
475 P. (2012). Lactate activates HIF-1 in oxidative but not in Warburg-phenotype human
476 tumor cells. PLoS One *7*, e46571.
477 Dobrovolny, P.L., and Bess, D. (2011). Optimized PCR-based detection of mycoplasma.
478 J Vis Exp.
479 Evans, M.J., and Kaufman, M.H. (1981). Establishment in culture of pluripotential cells
480 from mouse embryos. Nature *292*, 154-156.
481 Fischer, B., and Bavister, B.D. (1993). Oxygen tension in the oviduct and uterus of
482 rhesus monkeys, hamsters and rabbits. J Reprod Fertil *99*, 673-679.
483 Folmes, C.D., Nelson, T.J., Martinez-Fernandez, A., Arrell, D.K., Lindor, J.Z., Dzeja,
484 P.P., Ikeda, Y., Perez-Terzic, C., and Terzic, A. (2011). Somatic oxidative bioenergetics
485 transitions into pluripotency-dependent glycolysis to facilitate nuclear reprogramming.
486 Cell Metab *14*, 264-271.
487 Fujikura, J., Yamato, E., Yonemura, S., Hosoda, K., Masui, S., Nakao, K., Miyazaki Ji,
488 J., and Niwa, H. (2002). Differentiation of embryonic stem cells is induced by GATA
489 factors. Genes Dev *16*, 784-789.

490 Gatie, M.I., and Kelly, G.M. (2018). Metabolic profile and differentiation potential of
491 extraembryonic endoderm-like cells. Cell Death Discov *4*, 42.
492 Gu, W., Gaeta, X., Sahakyan, A., Chan, A.B., Hong, C.S., Kim, R., Braas, D., Plath, K.,
493 Lowry, W.E., and Christofk, H.R. (2016). Glycolytic Metabolism Plays a Functional Role
494 in Regulating Human Pluripotent Stem Cell State. Cell Stem Cell *19*, 476-490.
495 Halestrap, A.P. (1975). The mitochondrial pyruvate carrier. Kinetics and specificity for
496 substrates and inhibitors. Biochem J *148*, 85-96.
497 He, X., Chi, G., Li, M., Xu, J., Zhang, L., Song, Y., Wang, L., and Li, Y. (2020).
498 Characterisation of extraembryonic endoderm-like cells from mouse embryonic
499 fibroblasts induced using chemicals alone. Stem Cell Res Ther *11*, 157.
500 Hogan, B.L., Cooper, A.R., and Kurkinen, M. (1980). Incorporation into Reichert's
501 membrane of laminin-like extracellular proteins synthesized by parietal endoderm cells
502 of the mouse embryo. Dev Biol *80*, 289-300.
503 Houghton, F.D., Humpherson, P.G., Hawkhead, J.A., Hall, C.J., and Leese, H.J. (2003).
504 Na+, K+, ATPase activity in the human and bovine preimplantation embryo. Dev Biol
505 *263*, 360-366.
506 Huang da, W., Sherman, B.T., and Lempicki, R.A. (2009a). Bioinformatics enrichment
507 tools: paths toward the comprehensive functional analysis of large gene lists. Nucleic
508 Acids Res *37*, 1-13.
509 Huang da, W., Sherman, B.T., and Lempicki, R.A. (2009b). Systematic and integrative
510 analysis of large gene lists using DAVID bioinformatics resources. Nat Protoc *4*, 44-57.

511 Hui, S., Ghergurovich, J.M., Morscher, R.J., Jang, C., Teng, X., Lu, W., Esparza, L.A.,
512 Reya, T., Le, Z., Yanxiang Guo, J.*, et al.* (2017). Glucose feeds the TCA cycle via
513 circulating lactate. Nature *551*, 115-118.
514 Kunath, T., Arnaud, D., Uy, G.D., Okamoto, I., Chureau, C., Yamanaka, Y., Heard, E.,
515 Gardner, R.L., Avner, P., and Rossant, J. (2005). Imprinted X-inactivation in extra-
516 embryonic endoderm cell lines from mouse blastocysts. Development *132*, 1649-1661.
517 Langmead, B., and Salzberg, S.L. (2012). Fast gapped-read alignment with Bowtie 2.
518 Nat Methods *9*, 357-359.
519 Latham, T., Mackay, L., Sproul, D., Karim, M., Culley, J., Harrison, D.J., Hayward, L.,
520 Langridge-Smith, P., Gilbert, N., and Ramsahoye, B.H. (2012). Lactate, a product of
521 glycolytic metabolism, inhibits histone deacetylase activity and promotes changes in
522 gene expression. Nucleic Acids Res *40*, 4794-4803.
523 Li, B., and Dewey, C.N. (2011). RSEM: accurate transcript quantification from RNA-Seq
524 data with or without a reference genome. BMC Bioinformatics *12*, 323.
525 Love, M.I., Huber, W., and Anders, S. (2014). Moderated estimation of fold change and
526 dispersion for RNA-seq data with DESeq2. Genome Biol *15*, 550.
527 Mali, P., Chou, B.K., Yen, J., Ye, Z., Zou, J., Dowey, S., Brodsky, R.A., Ohm, J.E., Yu,
528 W., Baylin, S.B.*, et al.* (2010). Butyrate greatly enhances derivation of human induced
529 pluripotent stem cells by promoting epigenetic remodeling and the expression of
530 pluripotency-associated genes. Stem Cells *28*, 713-720.
531 Mathieu, J., and Ruohola-Baker, H. (2017). Metabolic remodeling during the loss and
532 acquisition of pluripotency. Development *144*, 541-551.

533 McDonald, A.C., Biechele, S., Rossant, J., and Stanford, W.L. (2014). Sox17-mediated
534 XEN cell conversion identifies dynamic networks controlling cell-fate decisions in
535 embryo-derived stem cells. Cell Rep *9*, 780-793.
536 Mulvey, C.M., Schroter, C., Gatto, L., Dikicioglu, D., Fidaner, I.B., Christoforou, A.,
537 Deery, M.J., Cho, L.T., Niakan, K.K., Martinez-Arias, A.*, et al.* (2015). Dynamic
538 Proteomic Profiling of Extra-Embryonic Endoderm Differentiation in Mouse Embryonic
539 Stem Cells. Stem Cells *33*, 2712-2725.
540 Niakan, K.K., Schrode, N., Cho, L.T., and Hadjantonakis, A.K. (2013). Derivation of
541 extraembryonic endoderm stem (XEN) cells from mouse embryos and embryonic stem
542 cells. Nat Protoc *8*, 1028-1041.
543 Nichols, J., Evans, E.P., and Smith, A.G. (1990). Establishment of germ-line-competent
544 embryonic stem (ES) cells using differentiation inhibiting activity. Development *110*,
545 1341-1348.
546 Nowotschin, S., Hadjantonakis, A.K., and Campbell, K. (2019). The endoderm: a
547 divergent cell lineage with many commonalities. Development *146*.
548 Paca, A., Seguin, C.A., Clements, M., Ryczko, M., Rossant, J., Rodriguez, T.A., and
549 Kunath, T. (2012). BMP signaling induces visceral endoderm differentiation of XEN cells
550 and parietal endoderm. Dev Biol *361*, 90-102.
551 Parenti, A., Halbisen, M.A., Wang, K., Latham, K., and Ralston, A. (2016). OSKM
552 Induce Extraembryonic Endoderm Stem Cells in Parallel to Induced Pluripotent Stem
553 Cells. Stem Cell Reports *6*, 447-455.

554 Polanski, R., Hodgkinson, C.L., Fusi, A., Nonaka, D., Priest, L., Kelly, P., Trapani, F.,
555 Bishop, P.W., White, A., Critchlow, S.E.*, et al.* (2014). Activity of the monocarboxylate
556 transporter 1 inhibitor AZD3965 in small cell lung cancer. Clin Cancer Res *20*, 926-937.
557 Ryu, J.M., and Han, H.J. (2011). L-threonine regulates G1/S phase transition of mouse
558 embryonic stem cells via PI3K/Akt, MAPKs, and mTORC pathways. J Biol Chem *286*,
559 23667-23678.
560 Seo, B.J., Choi, J., La, H., Habib, O., Choi, Y., Hong, K., and Do, J.T. (2020). Role of
561 mitochondrial fission-related genes in mitochondrial morphology and energy metabolism
562 in mouse embryonic stem cells. Redox Biol *36*, 101599.
563 Shimosato, D., Shiki, M., and Niwa, H. (2007). Extra-embryonic endoderm cells derived
564 from ES cells induced by GATA factors acquire the character of XEN cells. BMC Dev
565 Biol *7*, 80.
566 Soprano, D.R., Teets, B.W., and Soprano, K.J. (2007). Role of retinoic acid in the
567 differentiation of embryonal carcinoma and embryonic stem cells. Vitam Horm *75*, 69-
568 95.
569 Sutendra, G., Kinnaird, A., Dromparis, P., Paulin, R., Stenson, T.H., Haromy, A.,
570 Hashimoto, K., Zhang, N., Flaim, E., and Michelakis, E.D. (2014). A nuclear pyruvate
571 dehydrogenase complex is important for the generation of acetyl-CoA and histone
572 acetylation. Cell *158*, 84-97.
573 Tobias, I.C., Isaac, R.R., Dierolf, J.G., Khazaee, R., Cumming, R.C., and Betts, D.H.
574 (2018). Metabolic plasticity during transition to naive-like pluripotency in canine embryo-
575 derived stem cells. Stem Cell Res *30*, 22-33.

576 Tsogtbaatar, E., Landin, C., Minter-Dykhouse, K., and Folmes, C.D.L. (2020). Energy
577 Metabolism Regulates Stem Cell Pluripotency. Front Cell Dev Biol *8*, 87.
578 Vacanti, N.M., Divakaruni, A.S., Green, C.R., Parker, S.J., Henry, R.R., Ciaraldi, T.P.,
579 Murphy, A.N., and Metallo, C.M. (2014). Regulation of substrate utilization by the
580 mitochondrial pyruvate carrier. Mol Cell *56*, 425-435.
581 Wamaitha, S.E., del Valle, I., Cho, L.T., Wei, Y., Fogarty, N.M., Blakeley, P., Sherwood,
582 R.I., Ji, H., and Niakan, K.K. (2015). Gata6 potently initiates reprograming of pluripotent
583 and differentiated cells to extraembryonic endoderm stem cells. Genes Dev *29*, 1239-
584 1255.
585 Wang, J., Alexander, P., Wu, L., Hammer, R., Cleaver, O., and McKnight, S.L. (2009).
586 Dependence of mouse embryonic stem cells on threonine catabolism. Science *325*,
587 435-439.
588 Wessel, D., and Flugge, U.I. (1984). A method for the quantitative recovery of protein in
589 dilute solution in the presence of detergents and lipids. Anal Biochem *138*, 141-143.
590 Yanes, O., Clark, J., Wong, D.M., Patti, G.J., Sanchez-Ruiz, A., Benton, H.P., Trauger,
591 S.A., Desponts, C., Ding, S., and Siuzdak, G. (2010). Metabolic oxidation regulates
592 embryonic stem cell differentiation. Nat Chem Biol *6*, 411-417.
593 Ying, Q.L., Wray, J., Nichols, J., Batlle-Morera, L., Doble, B., Woodgett, J., Cohen, P.,
594 and Smith, A. (2008). The ground state of embryonic stem cell self-renewal. Nature *453*,
595 519-523.
596 Yuan, M., Breitkopf, S.B., Yang, X., and Asara, J.M. (2012). A positive/negative ion-
597 switching, targeted mass spectrometry-based metabolomics platform for bodily fluids,
598 cells, and fresh and fixed tissue. Nat Protoc *7*, 872-881.

599 Zhang, J., Nuebel, E., Daley, G.Q., Koehler, C.M., and Teitell, M.A. (2012). Metabolic
600 regulation in pluripotent stem cells during reprogramming and self-renewal. Cell Stem
601 Cell *11*, 589-595.
602 Zhou, W., Choi, M., Margineantu, D., Margaretha, L., Hesson, J., Cavanaugh, C., Blau,
603 C.A., Horwitz, M.S., Hockenbery, D., Ware, C.*, et al.* (2012). HIF1alpha induced switch
604 from bivalent to exclusively glycolytic metabolism during ESC-to-EpiSC/hESC transition.
605 EMBO J *31*, 2103-2116.

607 # Figure Legends:

608 **Figure 1. XEN cells are more sensitive to glycolytic inhibition.**

609 (A) Representative phase contrast images of ES and XEN cells cultured under control,
610 50mM 2-DG, and 2.5μM oligomycin. Solid arrows are indicative of round XEN morphology.
611 Dashed arrows are indicative of stellate XEN morphology. Scale bars = 100μm.

612 (B) Relative cell viability of ES and XEN cells under control, 50mM 2-DG and 2.5μM
613 oligomycin conditions.

614 (C) Total ATP levels in ES and XEN cells under control, 50mM 2-DG and 2.5μM
615 oligomycin conditions. (n = three biological replicates, ns = not significant, $^{**}P < 0.01$, $^{***}P$
616 <0.001).

617 **Figure 2. Intracellular metabolomic analysis of ES and XEN cells.**

618 (A) Volcano plots of differentially expressed metabolites from untargeted LC/GC-MS/MS
619 metabolomics of ES and XEN cells cultured under normal conditions. (fold change > 1
620 and $P < 0.05$). Metabolites enriched in ES cells are highlighted in purple (38 metabolites)
621 and metabolites enriched in XEN cells are highlighted in orange (105 metabolites).

622 (B, C) Levels of key intracellular metabolites generated by glycolysis, TCA cycle, and
623 amino acid detected by targeted LC/GC-MS/MS analysis of ES and XEN cells cultured
624 under normal conditions. Metabolites are expressed in ng and were normalized to cell
625 number. (n = three biological replicates, ns = not significant, $^{*}P < 0.05$, $^{**}P < 0.01$).

626 **Figure 3. Bulk transcriptomic and proteomic analysis of ES and XEN cells.**

627 (A) Volcano plots of differentially expressed genes from bulk RNA sequencing of ES and
628 XEN cells cultured under normal conditions. (fold change > 2 and adjusted $P < 0.01$).

629 Genes enriched in ES cells are highlighted in purple (2742 genes) and genes enriched in
630 XEN cells are highlighted in orange (1716 genes).
631 (B) Volcano plots of differentially expressed proteins from bulk proteomics of ES and XEN
632 cells cultured under normal conditions. (fold change > 2 and adjusted $P < 0.01$). Proteins
633 abundant in ES cells are highlighted in purple (165 proteins) and proteins abundant in
634 XEN cells are highlighted in orange (298 proteins).
635 (C) Dot plot representing enriched KEGG pathways in ES cells from transcriptomic
636 dataset.
637 (D) Dot plot representing enriched KEGG pathways in ES cells from proteomic dataset.
638 (E) Venn diagram of common targets from both transcriptomic and proteomic datasets
639 for specific KEGG pathways.
640 (F) Dot plot representing enriched KEGG pathways in XEN cells from transcriptomic
641 dataset.
642 (G) Dot plot representing enriched KEGG pathways in XEN cells from proteomic dataset.
643 **Figure 4. Levels of enzymes involved in pyruvate metabolism in ES and XEN cells.**
644 (A) Bar graph of qRT-PCR analysis of *Ldha/Ldhb* ratio in ES and XEN cells. *Rpl14* was
645 used a constitutive gene for qRT-PCR. (n = three biological replicates, $^{**}P < 0.01$).
646 (B) Representative immunoblot analysis showing levels of LDHA and LDHB in ES and
647 XEN cells. β-ACTIN served as a loading control. (n = three biological replicates).
648 (C) Bar graph of extracellular quantification of lactate levels in ES and XEN cells by
649 BioProfile®400 Chemical Analyzer. (n = three biological replicates, $^{*}P < 0.05$).
650 (D-E) Bar graph of expression level of *Mct1* and *Mct4* in ES and XEN cells. FPKM was
651 used for RNAseq data. (n = three biological replicates, $^{****}P < 0.0001$).

652 (F-I) Bar graph of FPKM of *Pdk1-4* in ES and XEN cells. (n = three biological replicates,
653 ns = not significant, $^{**}P$ <0.01, $^{****}P$ <0.0001).
654 (J) Representative immunoblot analysis showing levels of PDK1, PDK4, PDC-E1α^{pSer232},
655 PDC-E1α^{pSer293}, and PDC-E1α in ES and XEN cells. (n = three biological replicates).
656 (K-L) Bar graph of expression level of *Mpc1* and *Mpc2* in ES and XEN cells. FPKM was
657 used for RNAseq data. (n = three biological replicates, $^{***}P$ <0.001).
658 **Figure 5. Intracellular lactate enhances XEN differentiation *in vitro*.**
659 (A) Schematic diagram of glucose metabolism and the metabolic enzymes involved.
660 Green is indicative of treatments that increase intracellular lactate and red is indicative of
661 treatment that decrease intracellular lactate.
662 (B-C) Bar graph of expression level of *Oct4* and *Nanog* in ES cells in 2i-LIF with or without
663 50μM UK5099 for 48h. *Rpl14* was used a constitutive gene for qRT-PCR. (n = three
664 biological replicates, $^{*}P$ <0.05).
665 (D-E) Bar graph of expression level of *Gata6* and *Dab2* in ES cells induced towards a
666 XEN lineage with or without 50μM UK5099 for 96h. *Rpl14* was used a constitutive gene
667 for qRT-PCR. (n = three biological replicates, $^{*}P$ <0.05).
668 (F-G) Bar graph of expression level of *Oct4* and *Nanog* in ES cells in 2i-LIF with or without
669 250nM AZD3965 for 48h. *Rpl14* was used a constitutive gene for qRT-PCR. (n = three
670 biological replicates).
671 (H-I) Bar graph of expression level of *Gata6* and *Dab2* in ES cells induced towards a XEN
672 lineage with or without 250nM AZD3965 for 96h. *Rpl14* was used a constitutive gene for
673 qRT-PCR. (n = three biological replicates, $^{*}P$ <0.05).

674 (J-K) Bar graph of expression level of *Oct4* and *Nanog* in ES cells in 2i-LIF with or without
675 5mM L-lactate for 48h. *Rpl14* was used a constitutive gene for qRT-PCR. (n = three
676 biological replicates).
677 (L-M) Bar graph of expression level of *Gata6* and *Dab2* in ES cells induced towards a
678 XEN lineage with or without 5mM L-lactate for 96h. *Rpl14* was used a constitutive gene
679 for qRT-PCR. (n = three biological replicates, $^{*}P$ <0.05).
680 (N-O) Bar graph of expression level of *Oct4* and *Nanog* in ES cells in 2i-LIF with or without
681 5mM DCA for 48h. *Rpl14* was used a constitutive gene for qRT-PCR. (n = three biological
682 replicates, $^{*}P$ <0.05, $^{**}P$ <0.01).
683 (P-Q) Bar graph of expression level of *Gata6* and *Dab2* in ES cells induced towards a
684 XEN lineage with or without 5mM DCA for 96h. *Rpl14* was used a constitutive gene for
685 qRT-PCR. (n = three biological replicates, $^{*}P$ <0.05).
686 **Figure S1. Morphological and molecular analysis of ES and XEN cells *in vitro*.**
687 (A) A representative phase contrast micrograph of ES and XEN cells cultured under
688 maintenance conditions under free-feeder conditions.
689 (B) Immunoblot analysis of OCT4 (pluripotency marker) and DAB2, GATA6, and
690 KERATIN-8 (extraembryonic endoderm markers). β-ACTIN served as a loading control.
691 (C-D) Bar graph of expression level of *Oct4* and *Nanog* in ES and XEN cells under
692 maintenance conditions. *Rpl14* was used a constitutive gene for qRT-PCR. (n = three
693 biological replicates, $^{***}P$ <0.001).
694 (E-H) Bar graph of expression level of *Gata6*, *Sox7*, *Dab2*, and *Foxa2* in ES and XEN
695 cells under maintenance conditions. *Rpl14* was used a constitutive gene for qRT-PCR. (n
696 = three biological replicates, $^{*}P$ <0.05, $^{**}P$ <0.01).

697 **Figure S2. GO term analysis of ES and XEN cells.**

698 (A-B) Bar graph representing top 10 enriched GO biological processes terms in ES cells
699 from transcriptomic and proteomic dataset.

700 (C-D) Bar graph representing top 10 enriched GO biological processes terms in XEN cells
701 from transcriptomic and proteomic dataset.

702 (E-F) Bar graph representing top 10 enriched GO cellular compartments terms in ES cells
703 from transcriptomic and proteomic dataset.

704 (G-H) Bar graph representing top 10 enriched GO cellular compartments terms in XEN
705 cells from transcriptomic and proteomic dataset.

706 (I-J) Bar graph representing top 10 enriched GO molecular functions terms in ES cells
707 from transcriptomic and proteomic dataset.

708 (K-L) Bar graph representing top 10 enriched GO molecular functions terms in XEN cells
709 from transcriptomic and proteomic dataset.

710 **Figure S3. *In vitro* induction of ES cells towards the XEN lineage.**

711 (A) Schematic diagram of the methodology of cXEN induction *in* vitro.

712 (B-C) Bar graph of expression level of *Nanog* and *Oct4* in ES cells induced towards the
713 XEN lineage over 8 days. *Rpl14* was used a constitutive gene for qRT-PCR. (n = three
714 biological replicates).

715 (D-E) Bar graph of expression level of *Gata6* and *Dab2* in ES cells induced towards the
716 XEN lineage over 8 days. *Rpl14* was used a constitutive gene for qRT-PCR. (n = three
717 biological replicates).

Tables:

Table 1. Metabolites enriched in either ES or XEN cells based on untargeted/targeted metabolomics

ES	XEN
Choline	Indole
Dimethylglycine	Betaine
N-acetylputrescine	Purine
Cytidine	Methylcysteine
Acadesine	2-Aminooctanoic acid
Adenosine	Methionine sulfoxide
Guanosine	N-carbamoyl-L-aspartate
Aminoimidazole carboxamide ribonucleotide	N-acetyl-glutamine
Glycerate	N-acetyl-glutamate
Carbamoyl phosphate	Ng,NG-dimethyl-L-arginine
Glucono-D-lactone	N-acetyl-glucosamine
2-dehydro-D-gluconate	Carnosine
Uridine	Glycerophosphocholine
Inosine	1-Methyladenosine
Sedoheptulose-1,7-bisphosphate	dCMP
Dihydroxy-acetone-phosphate	dAMP
Ethanolamine	GMP
Acylcarnitine C6:0	S-adenosyl-L-methionine
	Glutathione disulfide
	Methylmalonic acid
	N-acetyl-L-alanine
	Orotate
	Allantoin
	Phenylpyruvate
	Phenyllactic acid
	Uric acid
	sn-glycerol-3-phosphate
	Myo-inositol
	Xanthurenic acid
	Deoxyribose-phosphate
	2,3-diphosphoglyceric acid
	Glutathione
	UDP-D-glucose
	UDP-N-acetyl-glucosamine
	Taurine
	a-ketoglutarate
	Phosphoenolpyruvate
	AMP
	Hydroxyproline
	Asparagine
	Kynurenine
	Sarcosine
	Acylcarnitine C2:0
	Acylcarnitine C3:0
	Acylcarnitine C4:0
	Acylcarnitine C5:0
	Acylcarnitine C14:0
	Acylcarnitine C16:0
	Acylcarnitine C16-OH
	Acylcarnitine C18:0
	Lactate
	Succinate
	2-hydroxygluterate
	Glucose-6-phosphate
	Fructose-6-phophate
	Alanine
	4-aminobutyrate
	Serine
	Proline
	Threonine
	Leucine
	Glutamate
	Methionine
	Histidine
	Arginine
	Citrulline
	Tyrosine
	Tryptophan

Figure 1

A

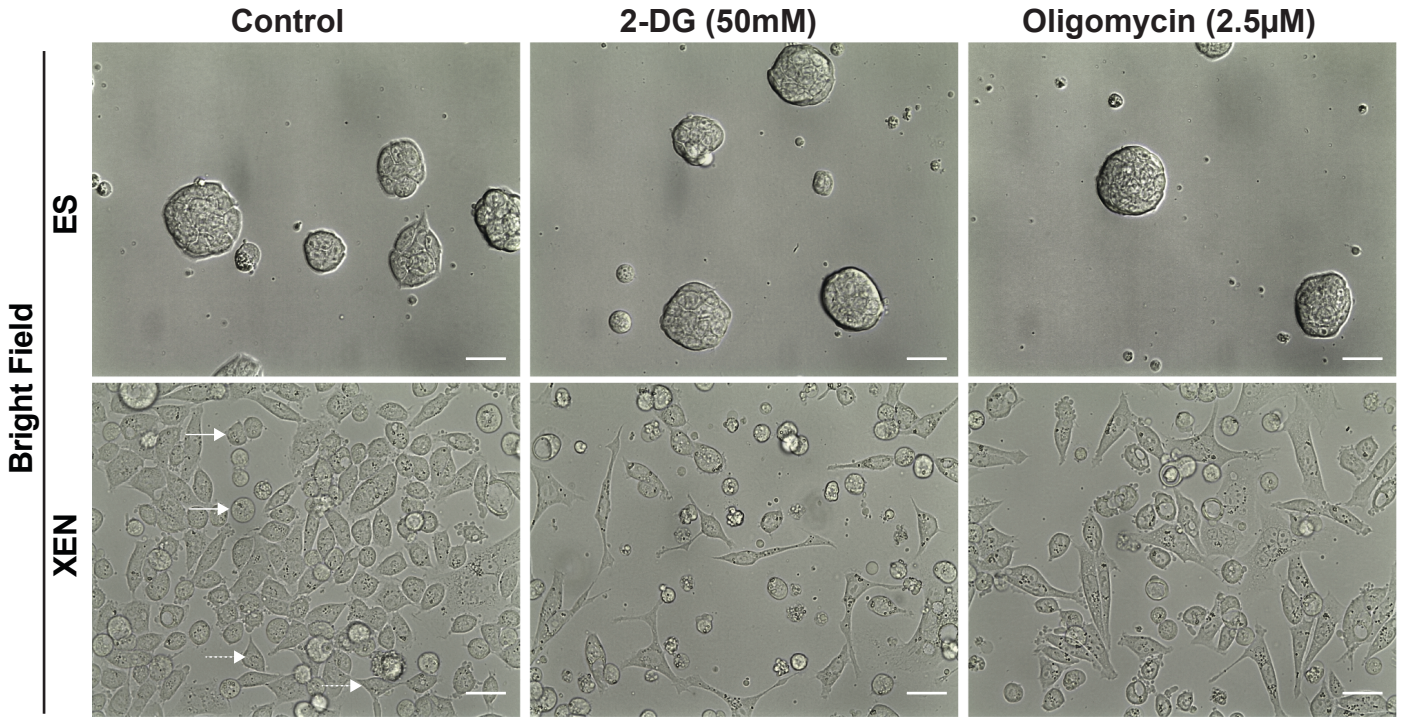
Control
2-DG (50mM)
Oligomycin (2.5μM)
Bright Field
ES
XEN

B

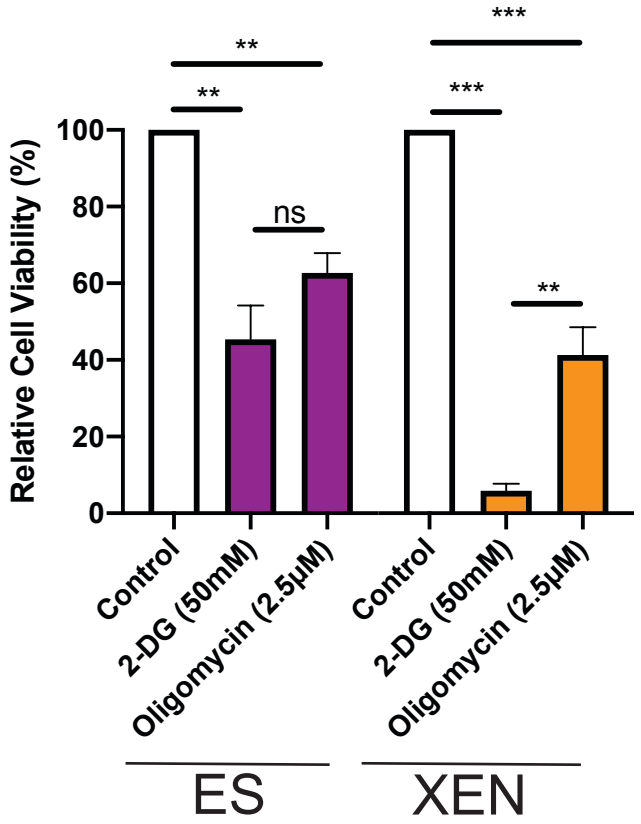
Relative Cell Viability (%)
100
80
60
40
20
0
**
**
ns
***
***
**
Control
2-DG (50mM)
Oligomycin (2.5μM)
Control
2-DG (50mM)
Oligomycin (2.5μM)
ES
XEN

C

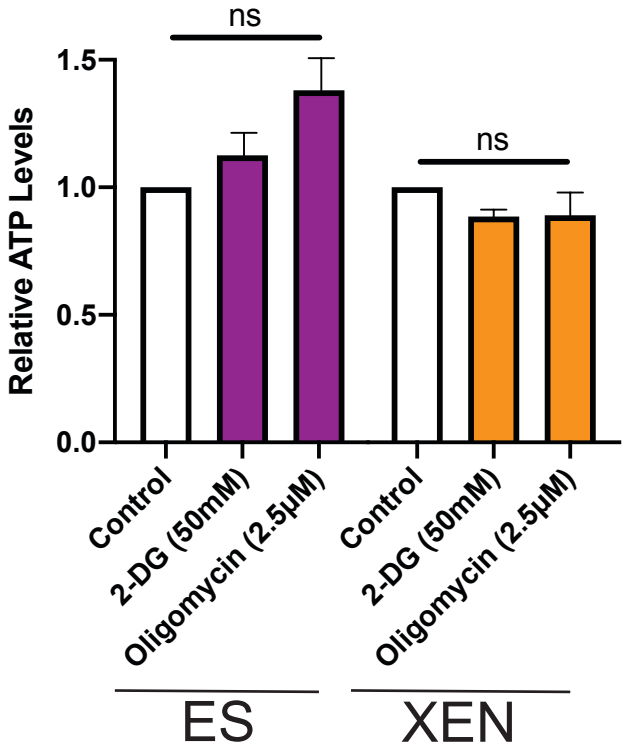
Relative ATP Levels
1.5
1.0
0.5
0.0
ns
ns
Control
2-DG (50mM)
Oligomycin (2.5μM)
Control
2-DG (50mM)
Oligomycin (2.5μM)
ES
XEN

Figure 2

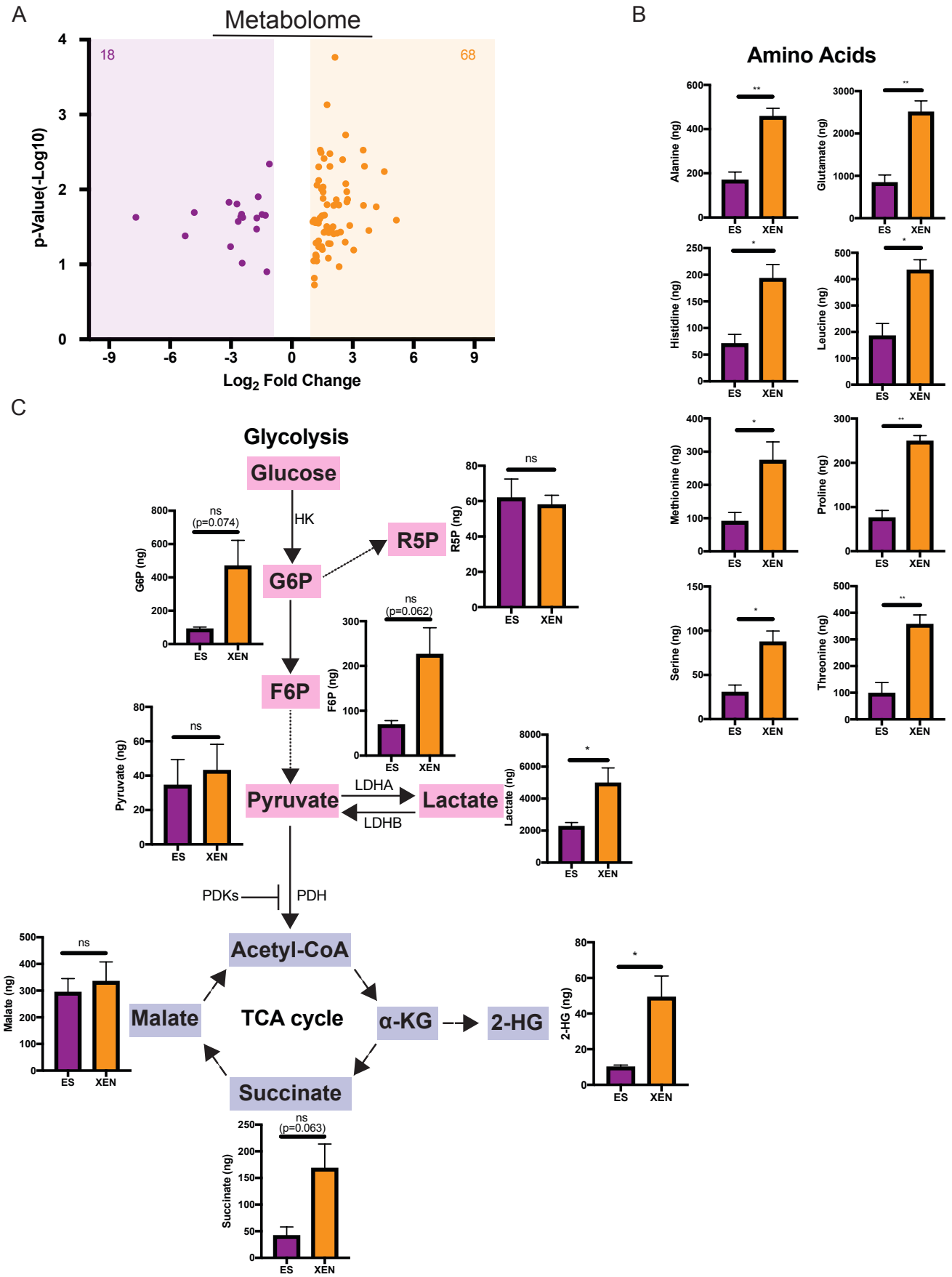
A
Metabolome
18
68
p-Value(-Log10)
Log2 Fold Change
B
Amino Acids
Alanine (ng)
Glutamate (ng)
Histidine (ng)
Leucine (ng)
Methionine (ng)
Proline (ng)
Serine (ng)
Threonine (ng)
ES
XEN
C
Glycolysis
Glucose
HK
G6P
R5P
F6P
Pyruvate
LDHA
LDHB
Lactate
PDKs
PDH
Acetyl-CoA
TCA cycle
Malate
α-KG
2-HG
Succinate
G6P (ng)
R5P (ng)
F6P (ng)
Pyruvate (ng)
Lactate (ng)
Malate (ng)
2-HG (ng)
Succinate (ng)
ns
(p=0.074)
(p=0.062)
(p=0.063)

Figure 3

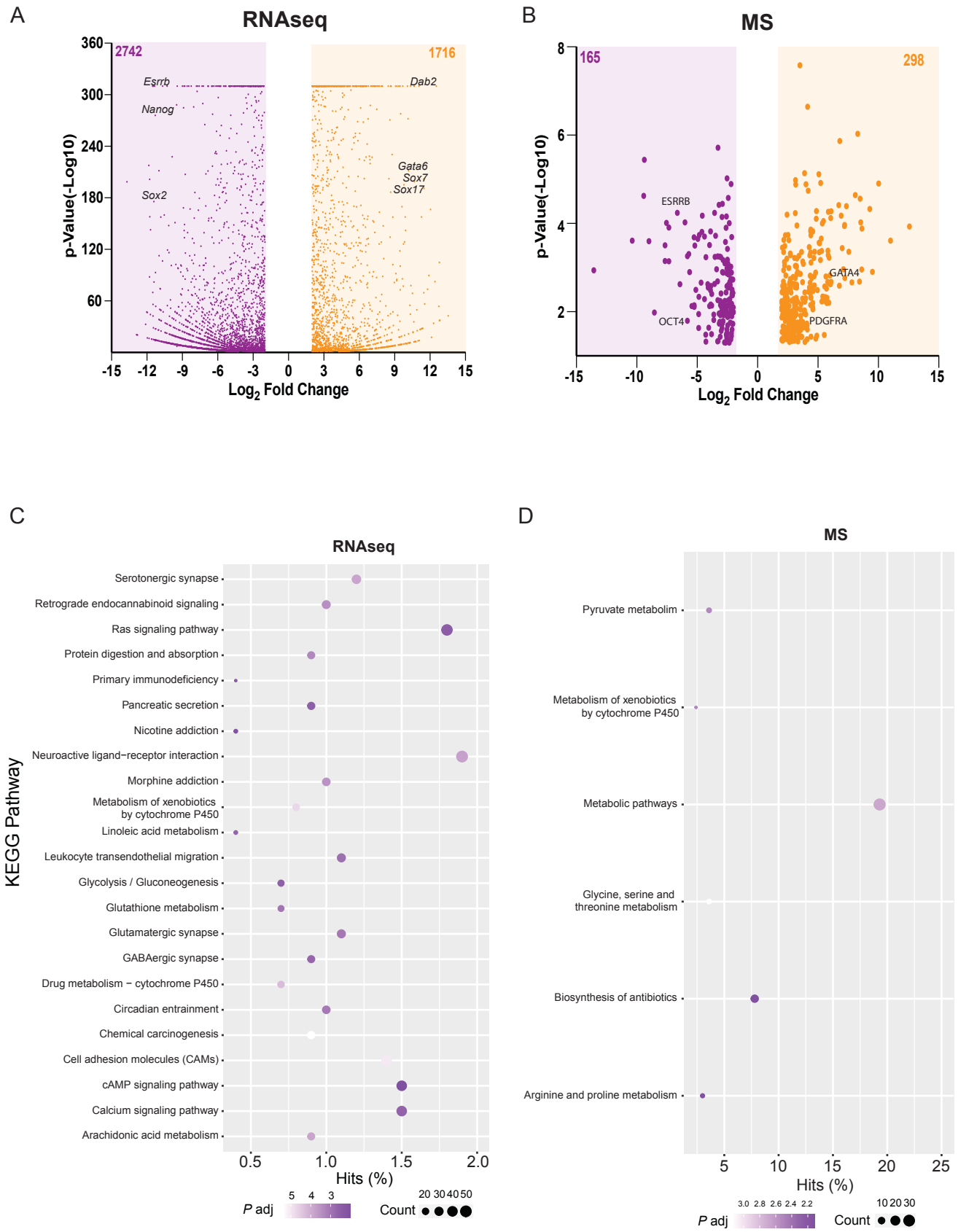
A
RNAseq
2742
1716
Esrrb
Nanog
Sox2
Dab2
Gata6
Sox7
Sox17
p-Value(-Log10)
Log2 Fold Change
B
MS
165
298
ESRRB
OCT4
GATA4
PDGFRA
p-Value(-Log10)
Log2 Fold Change
C
RNAseq
KEGG Pathway
Serotonergic synapse
Retrograde endocannabinoid signaling
Ras signaling pathway
Protein digestion and absorption
Primary immunodeficiency
Pancreatic secretion
Nicotine addiction
Neuroactive ligand−receptor interaction
Morphine addiction
Metabolism of xenobiotics by cytochrome P450
Linoleic acid metabolism
Leukocyte transendothelial migration
Glycolysis / Gluconeogenesis
Glutathione metabolism
Glutamatergic synapse
GABAergic synapse
Drug metabolism − cytochrome P450
Circadian entrainment
Chemical carcinogenesis
Cell adhesion molecules (CAMs)
cAMP signaling pathway
Calcium signaling pathway
Arachidonic acid metabolism
Hits (%)
P adj
Count
D
MS
Pyruvate metabolim
Metabolism of xenobiotics by cytochrome P450
Metabolic pathways
Glycine, serine and threonine metabolism
Biosynthesis of antibiotics
Arginine and proline metabolism
Hits (%)
P adj
Count

Figure 3 cont.

E

F

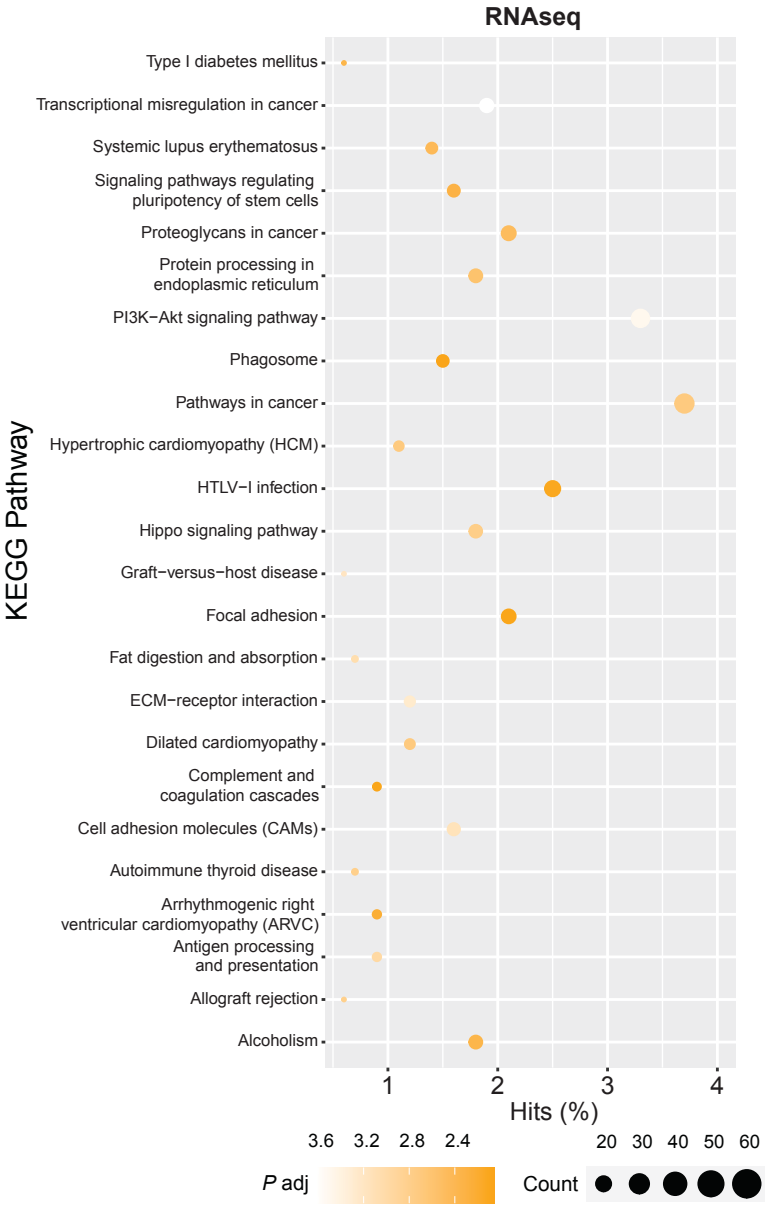

G

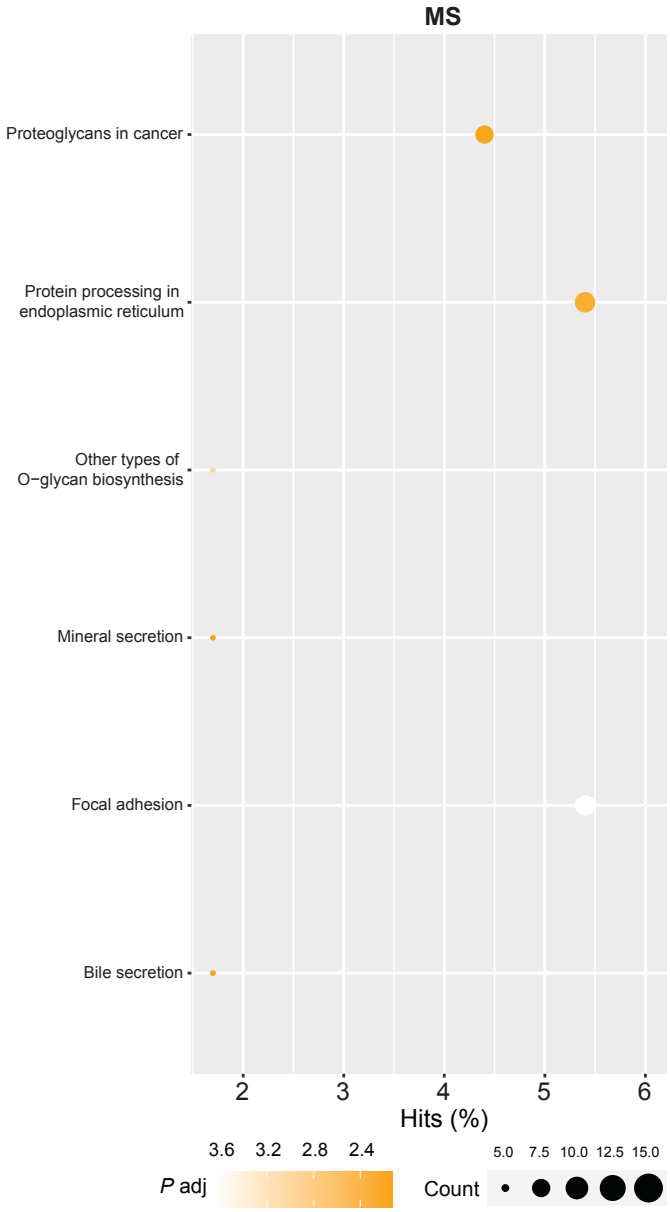

Figure 4

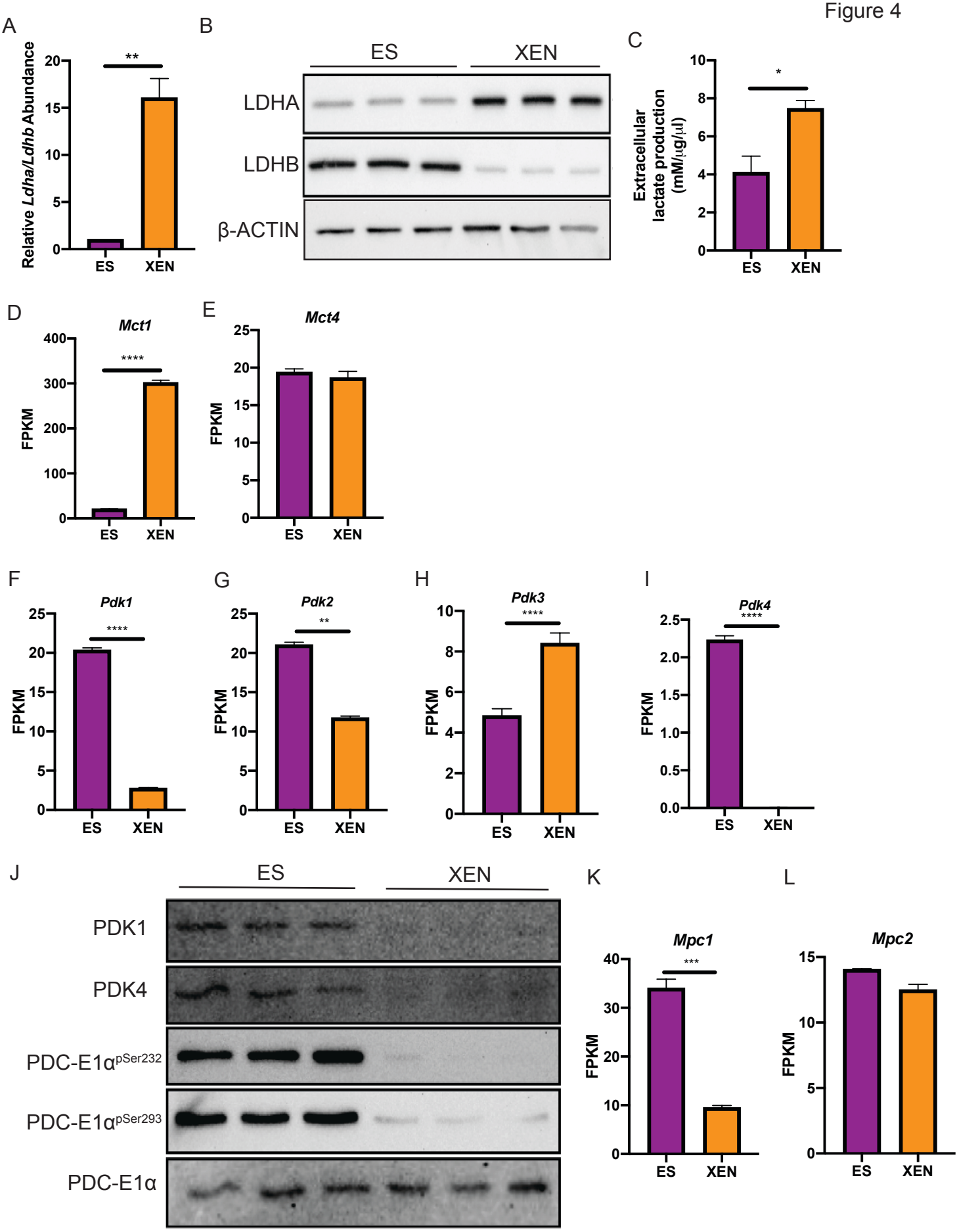
A
Relative Ldha/Ldhb Abundance
20
15
10
5
0
**
ES
XEN
B
ES
XEN
LDHA
LDHB
β-ACTIN
C
Extracellular lactate production (mM/μg/μl)
10
8
6
4
2
0
*
ES
XEN
D
Mct1
FPKM
400
300
200
100
0
****
ES
XEN
E
Mct4
FPKM
25
20
15
10
5
0
ES
XEN
F
Pdk1
FPKM
25
20
15
10
5
0
****
ES
XEN
G
Pdk2
FPKM
25
20
15
10
5
0
**
ES
XEN
H
Pdk3
FPKM
10
8
6
4
2
0
****
ES
XEN
I
Pdk4
FPKM
2.5
2.0
1.5
1.0
0.5
0.0
****
ES
XEN
J
ES
XEN
PDK1
PDK4
PDC-E1α pSer232
PDC-E1α pSer293
PDC-E1α
K
Mpc1
FPKM
40
30
20
10
0
***
ES
XEN
L
Mpc2
FPKM
15
10
5
0
ES
XEN

Figure 5

A

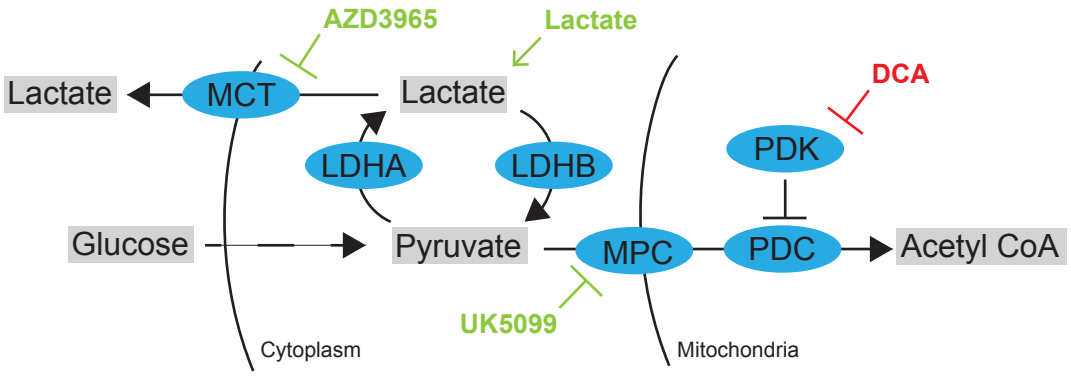

B

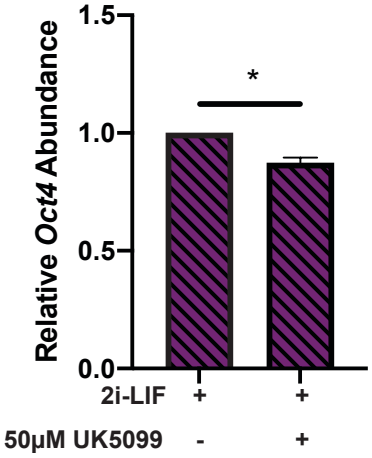

C

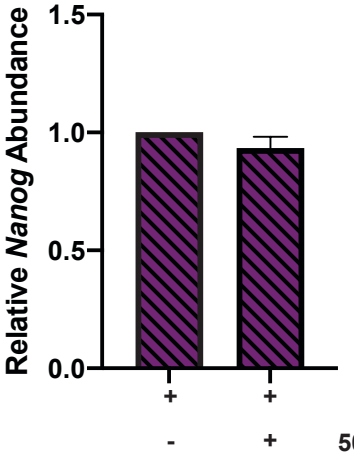

D

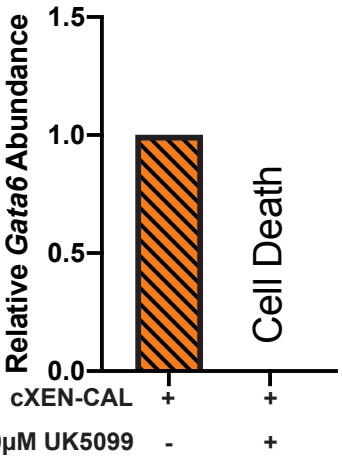

E

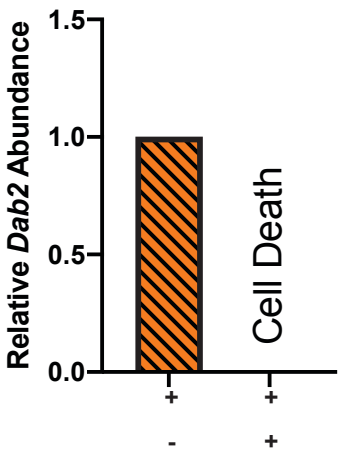

F

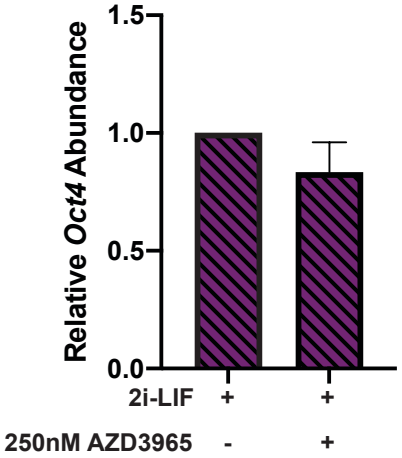

G

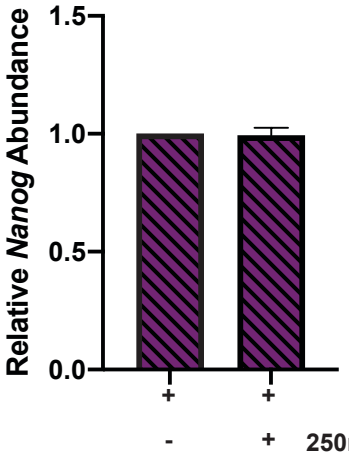

H

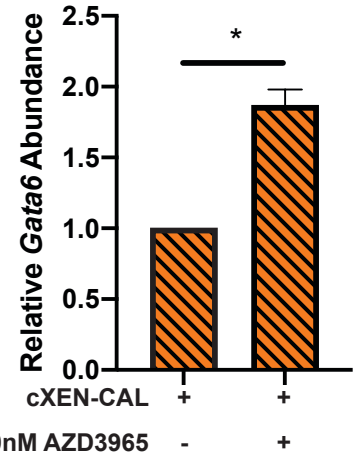

I

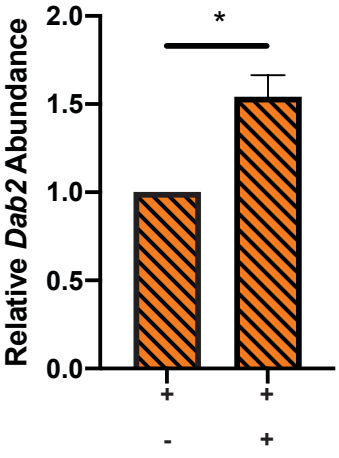

Figure 5 cont.

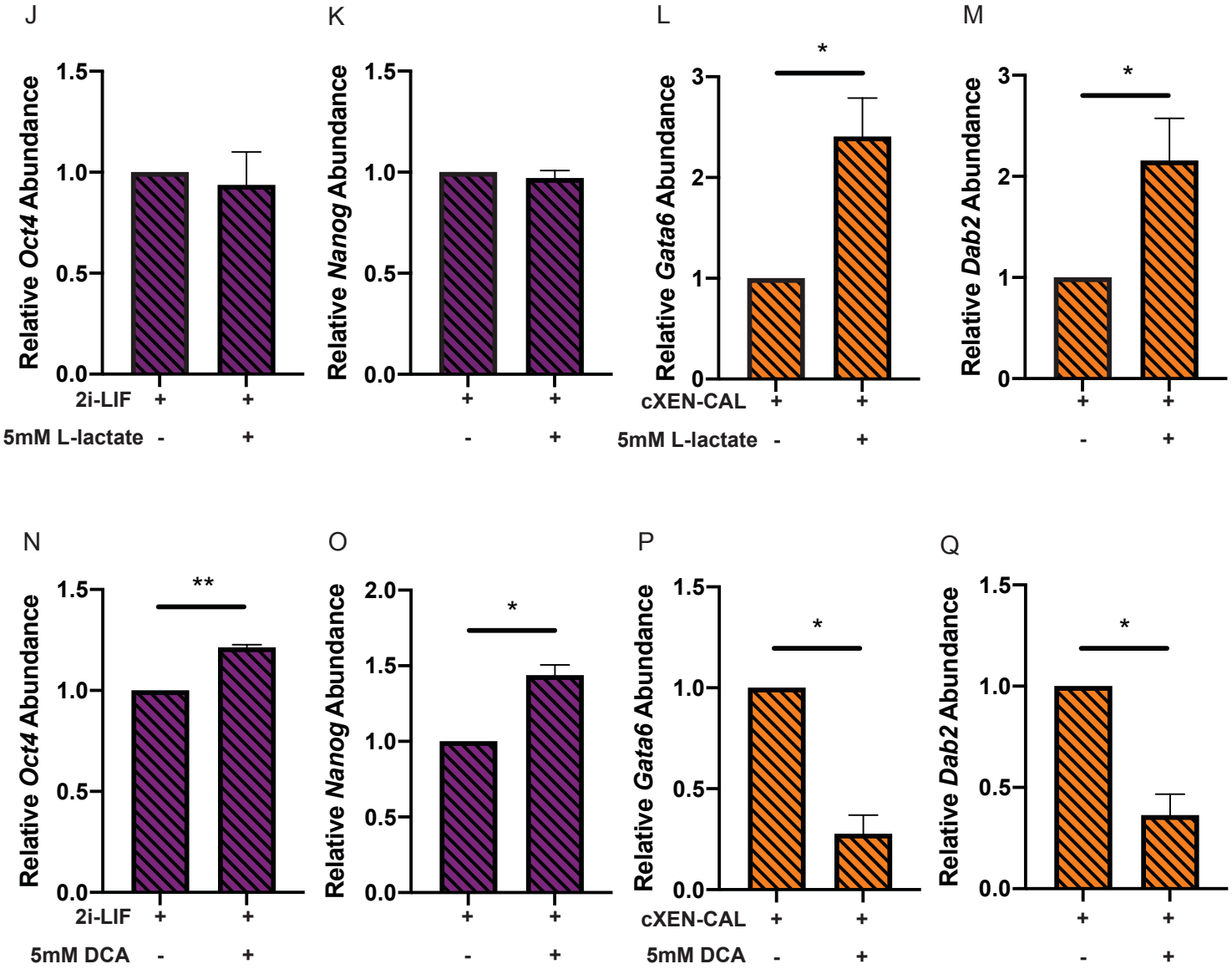

Figure S1

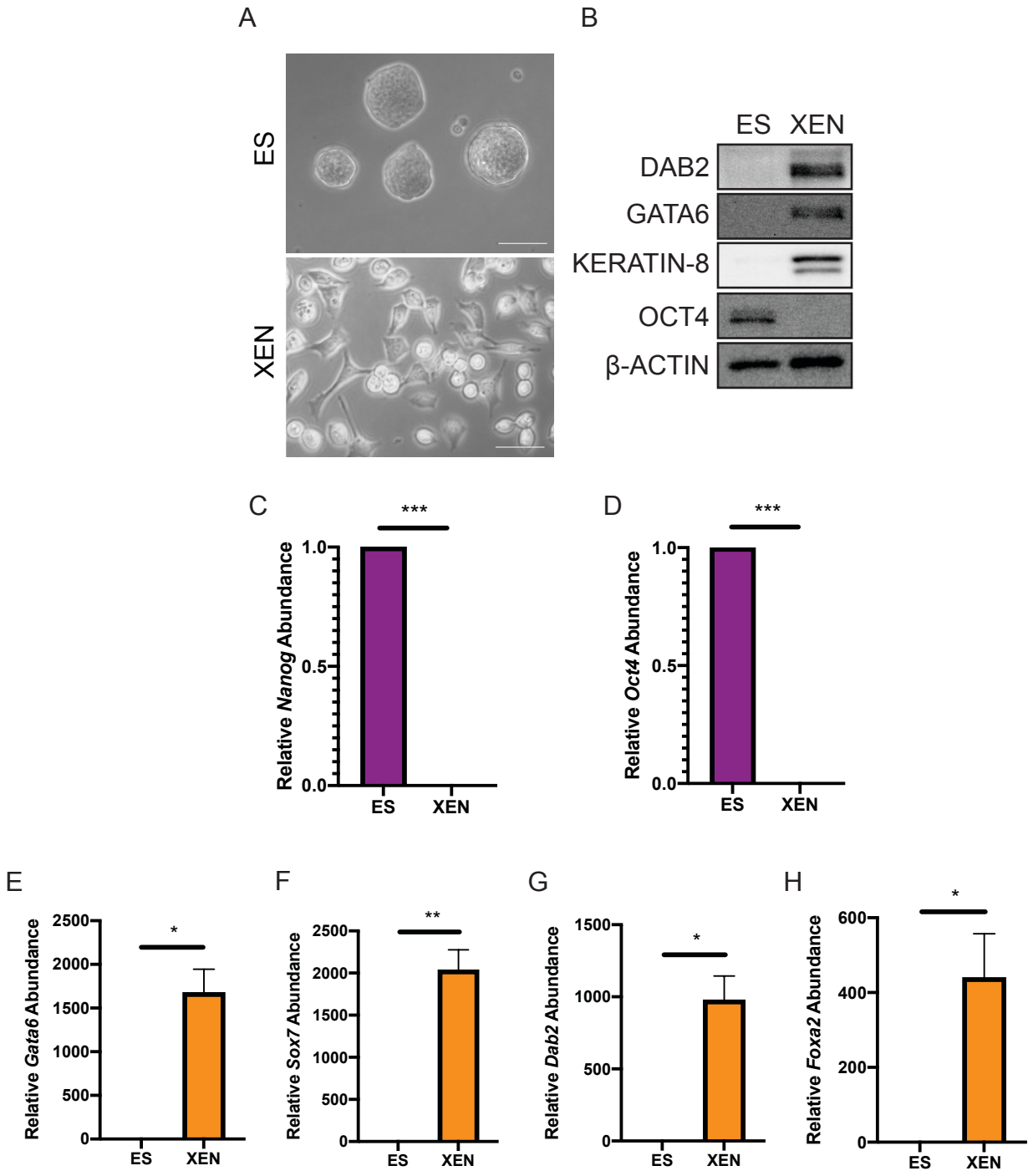
A
ES
XEN
B
ES XEN
DAB2
GATA6
KERATIN-8
OCT4
β-ACTIN
C
***
Relative Nanog Abundance
1.0
0.5
0.0
ES
XEN
D
***
Relative Oct4 Abundance
1.0
0.5
0.0
ES
XEN
E
*
Relative Gata6 Abundance
2500
2000
1500
1000
500
0
ES
XEN
F
**
Relative Sox7 Abundance
2500
2000
1500
1000
500
0
ES
XEN
G
*
Relative Dab2 Abundance
1500
1000
500
0
ES
XEN
H
*
Relative Foxa2 Abundance
600
400
200
0
ES
XEN

Figure S2

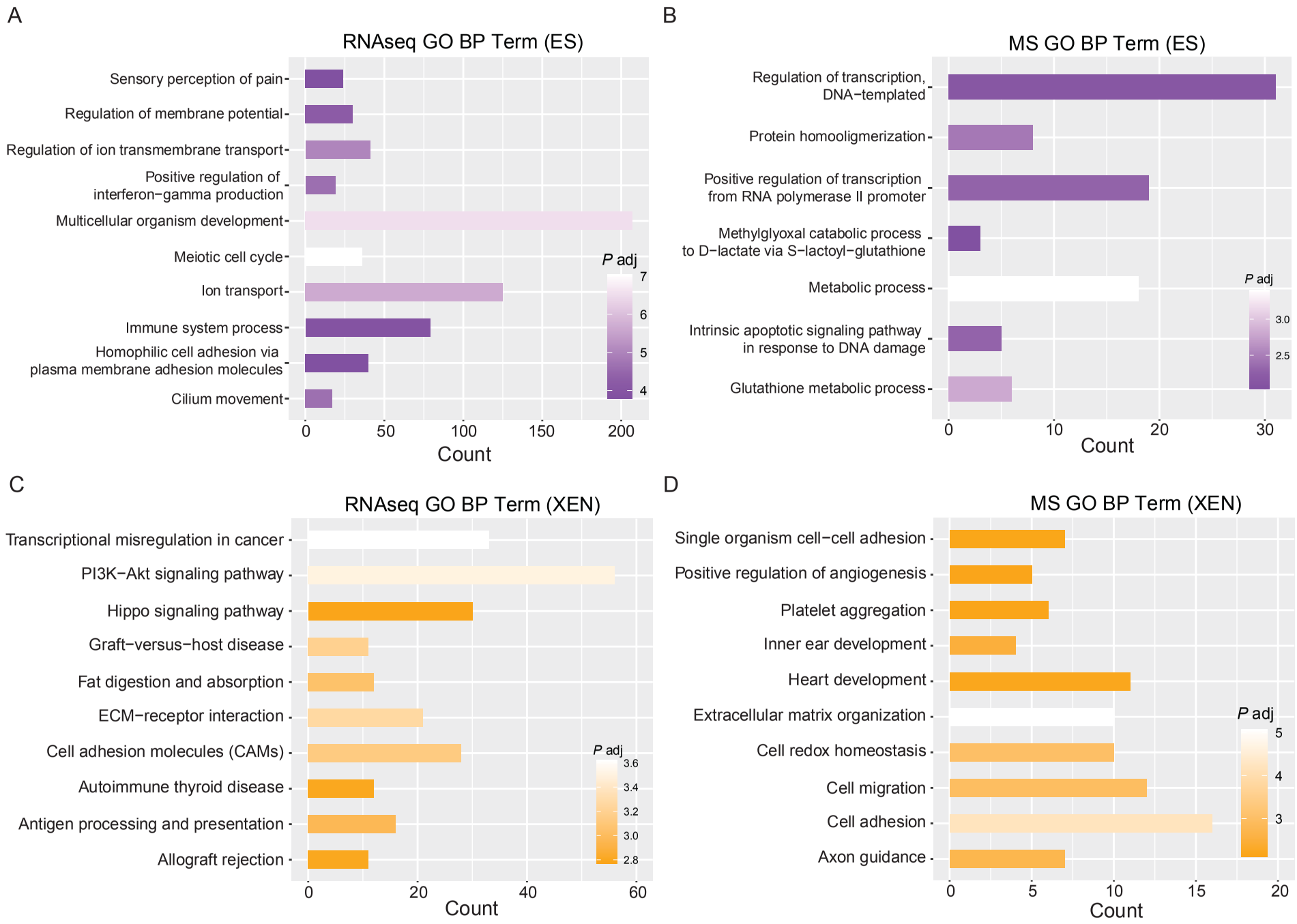
A
RNAseq GO BP Term (ES)
Sensory perception of pain
Regulation of membrane potential
Regulation of ion transmembrane transport
Positive regulation of interferon−gamma production
Multicellular organism development
Meiotic cell cycle
Ion transport
Immune system process
Homophilic cell adhesion via plasma membrane adhesion molecules
Cilium movement
0
50
100
150
200
Count
P adj
7
6
5
4
B
MS GO BP Term (ES)
Regulation of transcription, DNA−templated
Protein homooligmerization
Positive regulation of transcription from RNA polymerase II promoter
Methylglyoxal catabolic process to D−lactate via S−lactoyl−glutathione
Metabolic process
Intrinsic apoptotic signaling pathway in response to DNA damage
Glutathione metabolic process
0
10
20
30
Count
P adj
3.0
2.5
C
RNAseq GO BP Term (XEN)
Transcriptional misregulation in cancer
PI3K−Akt signaling pathway
Hippo signaling pathway
Graft−versus−host disease
Fat digestion and absorption
ECM−receptor interaction
Cell adhesion molecules (CAMs)
Autoimmune thyroid disease
Antigen processing and presentation
Allograft rejection
0
20
40
60
Count
P adj
3.6
3.4
3.2
3.0
2.8
D
MS GO BP Term (XEN)
Single organism cell−cell adhesion
Positive regulation of angiogenesis
Platelet aggregation
Inner ear development
Heart development
Extracellular matrix organization
Cell redox homeostasis
Cell migration
Cell adhesion
Axon guidance
0
5
10
15
20
Count
P adj
5
4
3

Figure S2

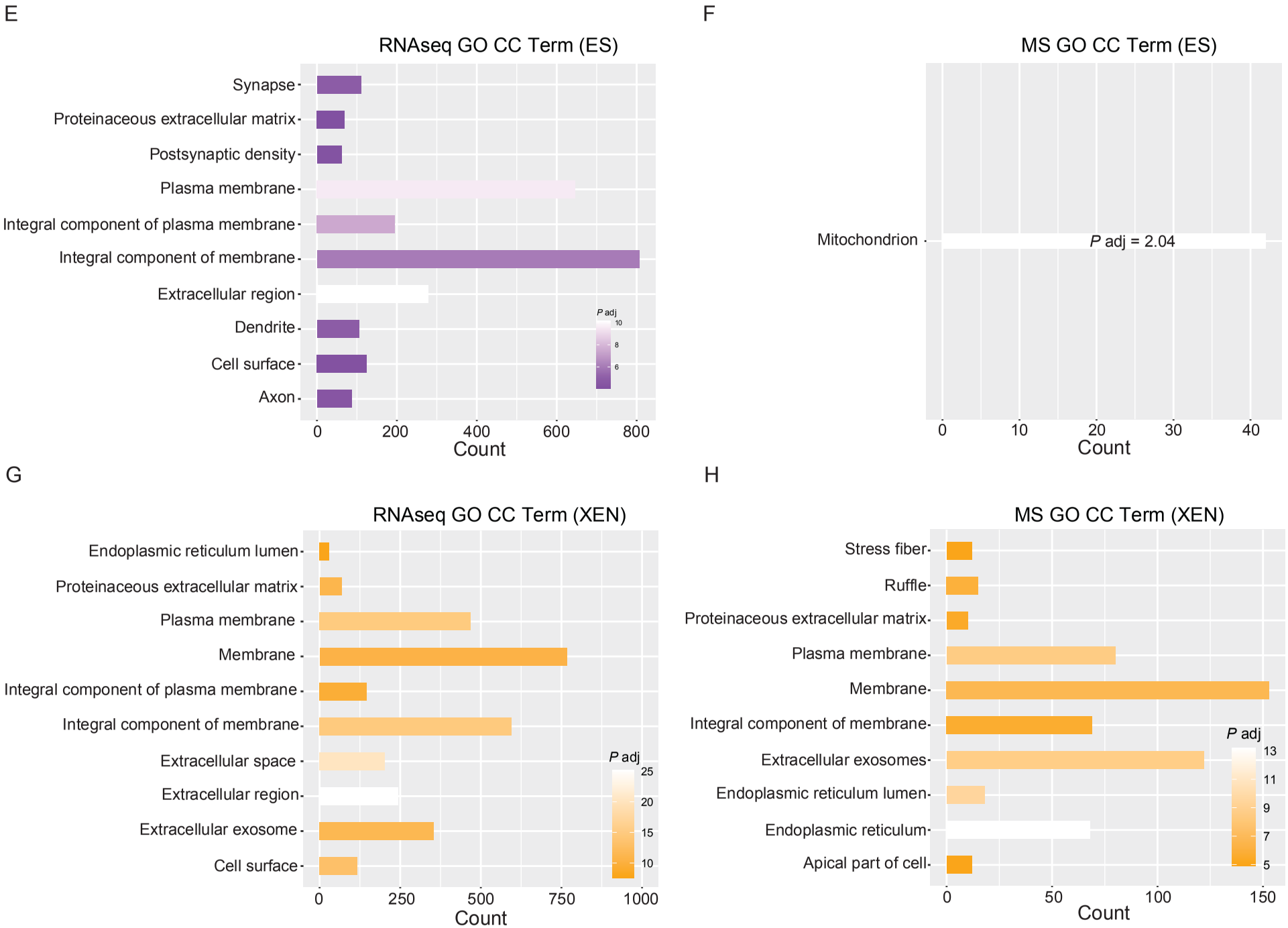
E
RNAseq GO CC Term (ES)
Synapse
Proteinaceous extracellular matrix
Postsynaptic density
Plasma membrane
Integral component of plasma membrane
Integral component of membrane
Extracellular region
Dendrite
Cell surface
Axon
P adj
10
8
6
0
200
400
600
800
Count
F
MS GO CC Term (ES)
Mitochondrion
P adj = 2.04
0
10
20
30
40
Count
G
RNAseq GO CC Term (XEN)
Endoplasmic reticulum lumen
Proteinaceous extracellular matrix
Plasma membrane
Membrane
Integral component of plasma membrane
Integral component of membrane
Extracellular space
Extracellular region
Extracellular exosome
Cell surface
P adj
25
20
15
10
0
250
500
750
1000
Count
H
MS GO CC Term (XEN)
Stress fiber
Ruffle
Proteinaceous extracellular matrix
Plasma membrane
Membrane
Integral component of membrane
Extracellular exosomes
Endoplasmic reticulum lumen
Endoplasmic reticulum
Apical part of cell
P adj
13
11
9
7
5
0
50
100
150
Count

Figure S2

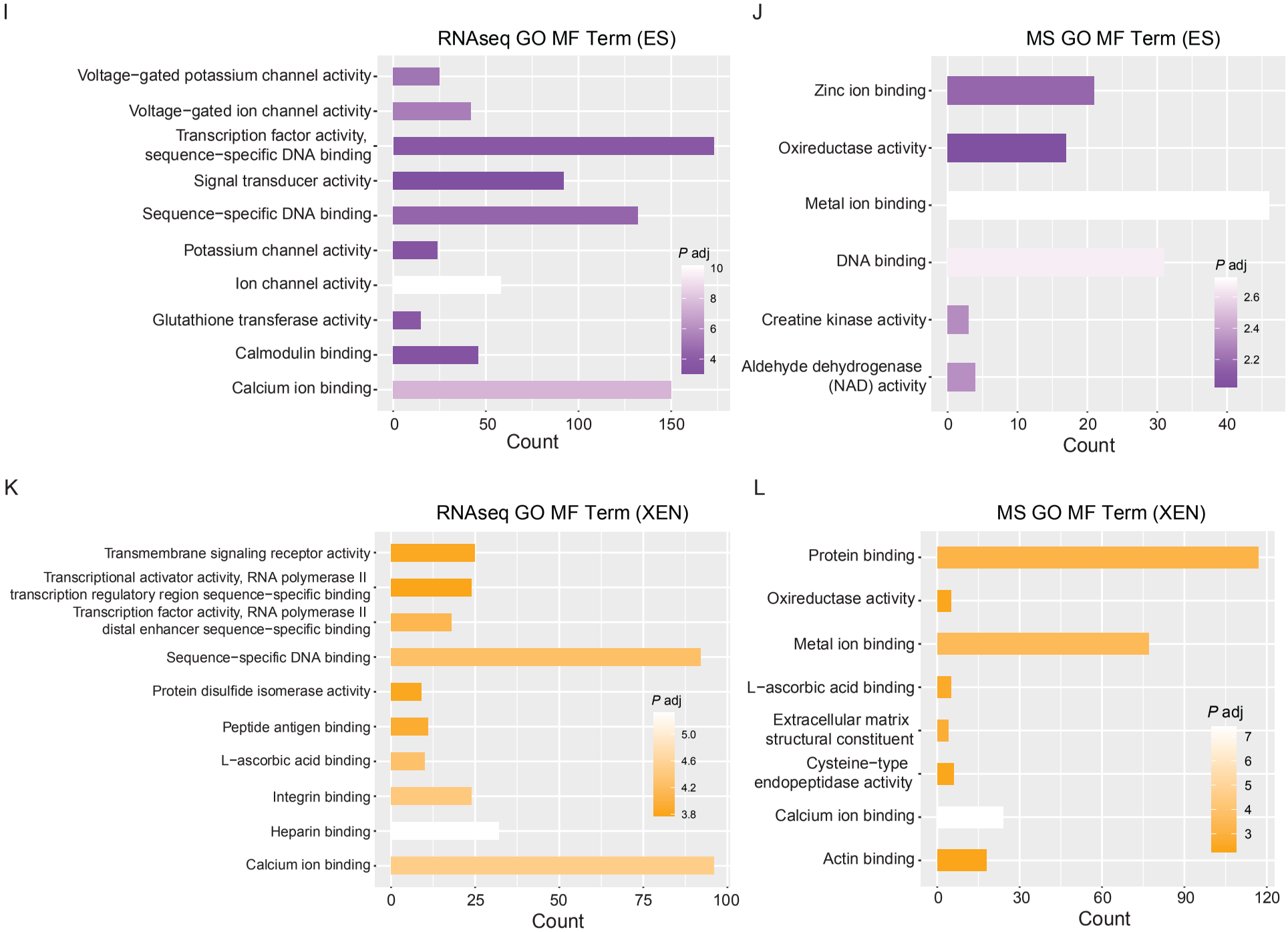
I
RNAseq GO MF Term (ES)
Voltage−gated potassium channel activity
Voltage−gated ion channel activity
Transcription factor activity, sequence−specific DNA binding
Signal transducer activity
Sequence−specific DNA binding
Potassium channel activity
Ion channel activity
Glutathione transferase activity
Calmodulin binding
Calcium ion binding
P adj
10
8
6
4
0
50
100
150
Count
J
MS GO MF Term (ES)
Zinc ion binding
Oxireductase activity
Metal ion binding
DNA binding
Creatine kinase activity
Aldehyde dehydrogenase (NAD) activity
P adj
2.6
2.4
2.2
0
10
20
30
40
Count
K
RNAseq GO MF Term (XEN)
Transmembrane signaling receptor activity
Transcriptional activator activity, RNA polymerase II transcription regulatory region sequence−specific binding
Transcription factor activity, RNA polymerase II distal enhancer sequence−specific binding
Sequence−specific DNA binding
Protein disulfide isomerase activity
Peptide antigen binding
L−ascorbic acid binding
Integrin binding
Heparin binding
Calcium ion binding
P adj
5.0
4.6
4.2
3.8
0
25
50
75
100
Count
L
MS GO MF Term (XEN)
Protein binding
Oxireductase activity
Metal ion binding
L−ascorbic acid binding
Extracellular matrix structural constituent
Cysteine−type endopeptidase activity
Calcium ion binding
Actin binding
P adj
7
6
5
4
3
0
30
60
90
120
Count

Figure S3

A

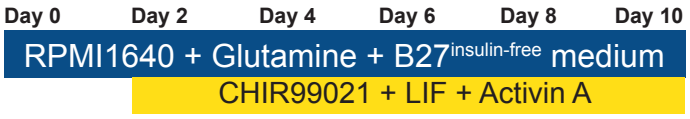

B

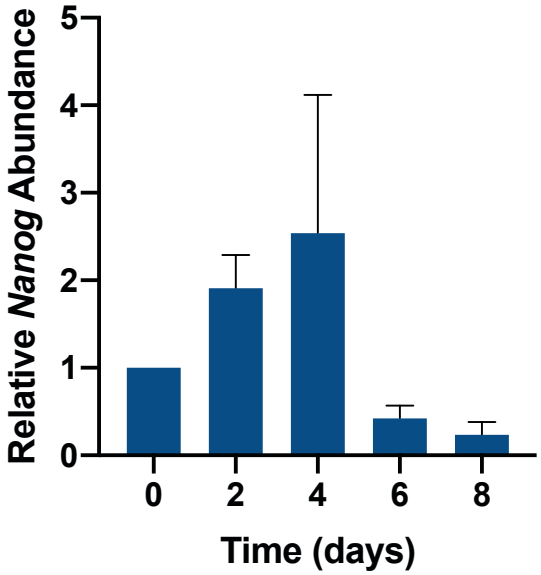

C

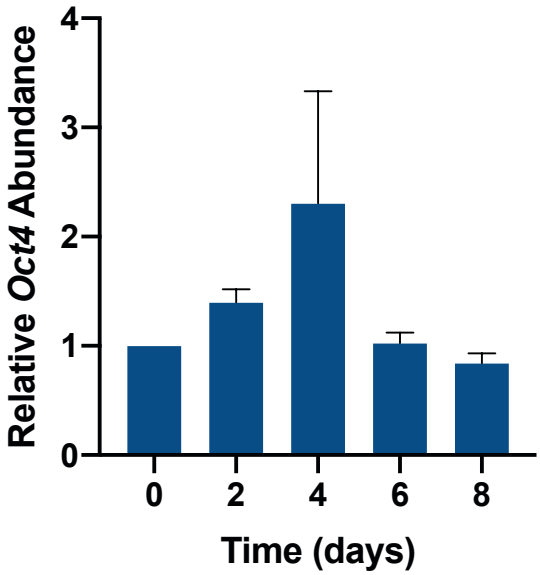

D

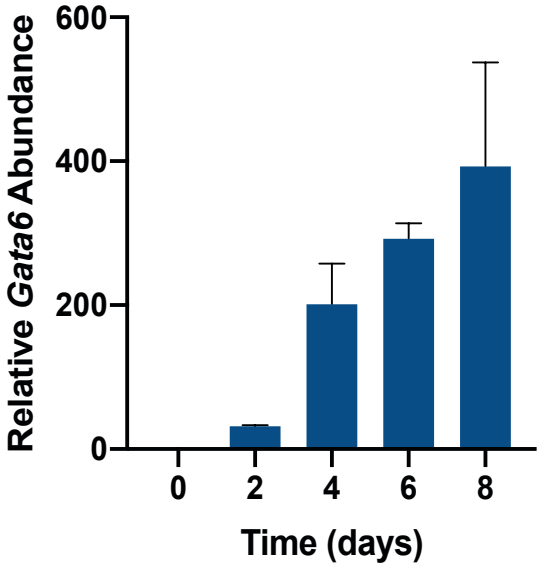
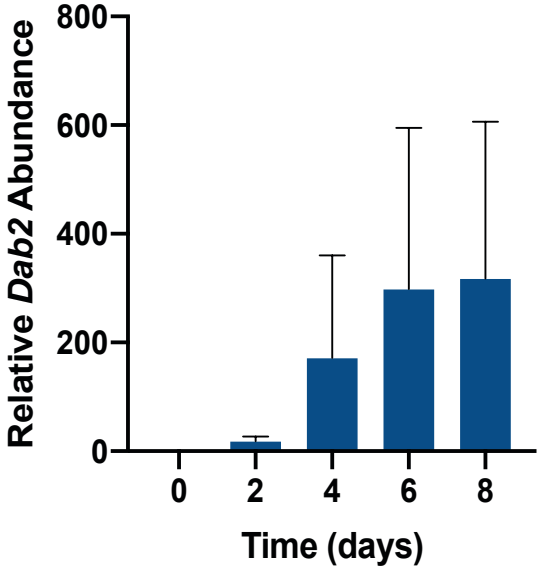
E